Latitudinal scaling of aggregation with abundance and its consequences for coexistence in species rich forests

Thorsten Wiegand*, Xugao Wang*, Samuel M. Fischer, Nathan J. B. Kraft, Norman A. Bourg, Warren Y. Brockelman, Guanghong Cao, Min Cao, Wirong Chanthorn, Chengjin Chu, Stuart Davies, Sisira Ediriweera, C. V. S. Gunatilleke, I. A. U. N. Gunatilleke, Zhanqing Hao, Robert Howe, Mingxi Jiang, Guangze Jin, W. John Kress, Buhang Li, Juyu Lian, Luxiang Lin, Feng Liu, Keping Ma, William McShea, Xiangcheng Mi, Jonathan A. Myers, Anuttara Nathalang, David A. Orwig, Guochun Shen, Sheng-Hsin Su, I-Fang Sun, Xihua Wang, Amy Wolf, Enrong Yan, Wanhui Ye, Yan Zhu & Andreas Huth

1. Thorsten Wiegand: Helmholtz Centre for Environmental Research GmbH – UFZ, Department of Ecological Modelling, Permoserstrasse 15, 04318 Leipzig; German Centre for Integrative Biodiversity Research (iDiv) Halle-Jena-Leipzig, Deutscher Platz 5e, 04103 Leipzig;
2. Xugao Wang: CAS Key Laboratory of Forest Ecology and Management, Institute of Applied Ecology Chinese Academy of Sciences, Shenyang, Liaoning;
3. Samuel M. Fischer: Helmholtz Centre for Environmental Research GmbH – UFZ, Department of Ecological Modelling, Permoserstrasse 15, 04318 Leipzig;
4. Nathan J. B. Kraft: Department of Ecology and Evolutionary Biology, University of California, Los Angeles, 621 Charles E. Young Drive South, Los Angeles, CA 90095;
5. Norman A. Bourg: U.S. Geological Survey, National Research Program – Eastern Branch, Reston, Virginia
6. Warren Y. Brockelman: National Biobank of Thailand (NBT), National Science and Technology Development Agency, Klong Luang, Pathum Thani
7. Guanghong Cao: Administration Bureau of Naban River Watershed National Nature Reserve, Jinghong, Yunnan 666100, Kunming
8. Min Cao: CAS Key Laboratory of Tropical Forest Ecology, Xishuangbanna Tropical Botanical Garden, Chinese Academy of Sciences, Kunming
9. Wirong Chanthorn: Department of Environmental Technology and Management, Faculty of Environment, Kasetsart University, 10900, Bangkok
10. Chengjin Chu: State Key Laboratory of Biocontrol, School of Ecology, Sun Yat-sen University, Guangzhou
11. Stuart Davies: Forest Global Earth Observatory (ForestGEO), Smithsonian Tropical Research Institute, P.O. Box 37012, Washington DC
12. Sisira Ediriweera: Department of Science and Technology, Uva Wellassa University, Badulla
13. C. V. Savitri Gunatilleke: Department of Botany, University of Peradeniya, Kandy
14. I. A. U. Nimal Gunatilleke: Department of Botany, University of Peradeniya, Kandy
15. Zhanqing Hao: School of Ecology and Environment, Northwestern Polytechnical University, Xi'an
16. Robert Howe: Department of Natural and Applied Sciences, University of Wisconsin–Green Bay, 2420 Nicolet Drive, Green Bay, Wisconsin
17. Mingxi Jiang: Key Laboratory of Aquatic Botany and Watershed Ecology, Wuhan Botanical Garden, Chinese Academy of Sciences, Wuhan
18. Guangze Jin: Center for Ecological Research, Northeast Forestry University, Harbin
19. W. John Kress: Department of Botany, National Museum of Natural History, Smithsonian Institution, Washington, DC

20. Buhang Li: State Key Laboratory of Biocontrol, School of Ecology, Sun Yat-sen University, Guangzhou
21. Juyu Lian: Key Laboratory of Vegetation Restoration and Management of Degraded Ecosystems, South China Botanical Garden, Chinese Academy of Sciences, 510650, Guangzhou
22. Luxiang Lin: CAS Key Laboratory of Tropical Forest Ecology, Xishuangbanna Tropical Botanical Garden, Chinese Academy of Sciences, Kunming
23. Feng Liu: Yunnan Academy of Forestry and Grassland, Kunming 650201
24. Keping Ma: State Key Laboratory of Vegetation and Environmental Change, Institute of Botany, Chinese Academy of Sciences, 20 Nanxincun, Xiangshan, Beijing
25. William McShea: Conservation Ecology Center, Smithsonian Conservation Biology Institute, Front Royal, Virginia
26. Xiangcheng Mi: State Key Laboratory of Vegetation and Environmental Change, Institute of Botany, Chinese Academy of Sciences, 20 Nanxincun, Xiangshan, Beijing
27. Jonathan A. Myers: Department of Biology, Washington University in St. Louis, St. Louis, Missouri
28. Anuttara Nathalang, National Biobank of Thailand (NBT), National Science and Technology Development Agency, Klong Luang, Pathum Thani.
29. David A. Orwig: Harvard Forest, Harvard University, Petersham, Massachusetts
30. Guochun Shen: Zhejiang Tiantong Forest Ecosystem National Observation and Research Station, School of Ecological and Environmental Sciences, East China Normal University, Shanghai
31. Sheng-Hsin Su: Taiwan Forestry Research Institute, Taipei
32. I-Fang Sun: Center for Interdisciplinary Research on Ecology and Sustainability, National Dong Hwa University, Hualien
33. Xihua Wang: Zhejiang Tiantong Forest Ecosystem National Observation and Research Station, School of Ecological and Environmental Sciences, East China Normal University, Shanghai
34. Amy Wolf: Department of Natural and Applied Sciences, University of Wisconsin–Green Bay, 2420 Nicolet Drive, Green Bay, Wisconsin
35. Enrong Yan: Zhejiang Tiantong Forest Ecosystem National Observation and Research Station, School of Ecological and Environmental Sciences, East China Normal University, Shanghai
36. Wanhui Ye: Key Laboratory of Vegetation Restoration and Management of Degraded Ecosystems, South China Botanical Garden, Chinese Academy of Sciences, 510650, Guangzhou
37. Yan Zhu: State Key Laboratory of Vegetation and Environmental Change, Institute of Botany, Chinese Academy of Sciences, 20 Nanxincun, Xiangshan, Beijing
38. Andreas Huth: Helmholtz Centre for Environmental Research GmbH – UFZ, Department of Ecological Modelling, Permoserstrasse 15, 04318 Leipzig; German Centre for Integrative Biodiversity Research (iDiv) Halle-Jena-Leipzig, Deutscher Platz 5e, 04103 Leipzig; University Osnabrueck, Institute of Environmental Systems Research, Barbarastrasse 12, 49076 Osnabrueck.

*Correspondence should be addressed to: thorsten.wiegand@ufz.de and wangxg@iae.ac.cn

Abstract

The search for simple principles underlying the complex spatial structure and dynamics of plant communities is a long-standing challenge in ecology[1-6]. In particular, the relationship between the spatial distribution of plants and species coexistence is challenging to resolve in species-rich communities[7-9]. Analysing the spatial patterns of tree species in 21 large forest plots, we find that rare species tend to be more spatially aggregated than common species, and a latitudinal gradient in the strength of this negative correlations that increases from tropical to temperate forests. Our analysis suggests that latitudinal gradients in animal seed dispersal[10] and mycorrhizal associations[11,12,13] may jointly generate this intriguing pattern. To assess the consequences of negative aggregation-abundance correlations for species coexistence, we present here a framework to incorporate the observed spatial patterns into population models[8] along with an analytical solution for the local extinction risk[14] of species invading from low abundances in dependence of spatial structure, demographic parameters, and immigration. For example, the stabilizing effect of the observed spatial patterns reduced the local extinction risk of species when rare almost by a factor of two. Our approach opens up new avenues for integrating observed spatial patterns into mathematical theory, and our findings demonstrate that spatial patterns, such as species aggregation and segregation, can contribute substantially to coexistence in species-rich communities. This underscores the need to understand the interactions between multiple ecological processes and spatial patterns in greater detail.

Main Text

Tropical forests have been investigated by ecologists for decades, but their high species richness still remains a key challenge for ecological theory[1-6,15]. Although a large number of studies have been devoted to this issue, mechanistic connections among key features of forests and species coexistence are not understood[7-9]. One key feature is the widespread spatial aggregation of tree species, which has been used for long to infer mechanisms contributing to coexistence in tropical forests[16-21] because aggregation is related to ecological processes such as negative conspecific density dependence[16,17,21,22], dispersal limitation[2,23], distance-decay[20], mycorrhizal associations[11,12,13], and habitat filtering[24,25]. Conspecific spatial aggregation Ω is usually defined as the average density D of conspecific trees in neighbourhoods around each individual tree, divided by the mean tree density λ of the species in the plot[19,25]. Hence, Ω describes the extent to which trees of the same species tend to occur in spatial clusters. Theoretical and observational studies suggest that conspecific aggregation should be related to species abundance, with rarer species showing higher

levels of aggregation[8,18,19,20,26,27,28], whereas other studies find only weak relationships between aggregation and species abundance[29] (Supplementary Text).

From a theoretical perspective, different aggregation-abundance relationships are possible. At one extreme, when clusters form mostly near adults (e.g., due to short-distance dispersal[7,8,26] and/or mycorrhizal associations[11,12,13]), the density D of conspecific trees in the neighbourhood of individual trees is similar for rare and common species, but rarer species have fewer clusters (Fig. 1a versus 1b). Thus, aggregation (i.e., $\Omega=D/\lambda$[19,25]) increases if abundance and therefore mean tree density λ decrease. At the other extreme, when local clusters are created away from conspecific adults[8] (e.g., due to clumped animal seed dispersal, canopy gaps or edaphic habitat conditions[24,30,31,32,33]), fewer seeds will reach the cluster locations when the species is rarer. This makes the neighbourhood density D proportional to abundance and thus aggregation Ω independent of abundance (Fig. 1a versus 1c).

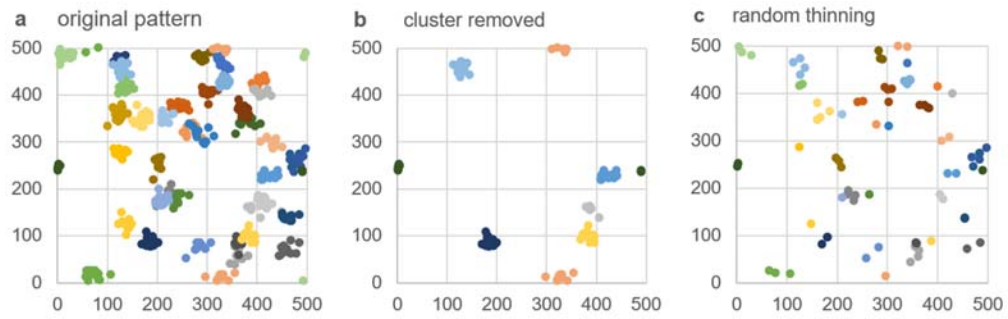

Fig. 1. Different responses of conspecific spatial aggregation to changes in abundance. a, clustered pattern of an abundant species with N = 500 individuals with mean neighbourhood density D = 0.012, mean tree density λ= 0.002, and aggregation $\Omega = D/\lambda$ = 5.8 (colours represent different clusters of individuals of the same species), **b,** entire clusters of the pattern in a) were removed (N = 100) to maintain the neighbourhood density D, but since λ was reduced by factor 1/5, aggregation increased 5 times (Ω = 26.9). **c,** 400 individuals of the pattern in a) were randomly removed to approximately maintain aggregation Ω = 4.8 (i.e., both, D and λ were reduced by the same factor 1/5).

Given the links between conspecific aggregation, negative density dependence and coexistence[7,8,9,22,26], the aggregation-abundance relationship may be related to the latitudinal diversity gradient[34]. Here, we conduct a comprehensive analysis of how spatial neighbourhood patterns of trees derived from large forest inventories[6] and the relationship of aggregation and abundance change with latitude. We propose underlying mechanisms, and integrate our results into mathematical theory to investigate how the aggregation-abundance relationship may affect species coexistence (Box 1).

While aggregation can be defined in a variety of ways[18,19,25,29,35], we use an upscaling approach[8] to derive biologically motivated measures of spatial patterns (such as aggregation) from established approaches to model the effect of neighbours on the performance of individual plants[36,37] (Box 1). We exemplify our new theory for neighbourhood crowding competition, where tree survival is reduced in areas of high tree neighbourhood density via competition for space, light or nutrients[38], or through natural enemies[16,17].

Box 1. Crowding indices, aggregation, segregation, and their link with macroscale dynamics

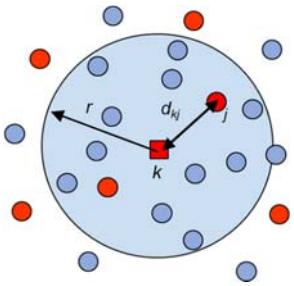

	individual level	population level	
conspecific:	$C_{kf} = \sum_{j=1}^{n_f} \frac{1}{d_{kj}}$	aggregation $\Rightarrow k_{ff} = \overline{C_{kf}}/(c\, N_f)$	(a)
heterospecific:	$H_{kf} = \sum_{i \neq f} \sum_{j=1}^{n_i} \frac{1}{d_{kj}}$	segregation $\Rightarrow k_{fh} = \overline{H_{kf}}/(c \sum_{i \neq f} N_i)$	(b)
niche differences:	$I_{kf} = \sum_{i \neq f} \sum_{j=1}^{n_i} (\frac{\beta_{fi}}{\beta_{ff}}) \frac{1}{d_{kj}}$	mean competition strength $B_f = \overline{I_{kf}}\ /\overline{H_{kf}}$ $\Rightarrow k_{fh}\, B_f = \overline{I_{kf}}\ /\ (c \sum_{s \neq f} N_s)$	(c1) (c2)
survival:	$s_{kf} = s_f e^{-\beta_{ff}(C_{kf} + I_{kf})}$	$\Rightarrow \bar{s}_f = s_f e^{-\beta_{ff}(\gamma_{ff}\overline{C_{kf}} + \gamma_{f\beta}\overline{I_{kf}})}$	(d)

Following earlier work on **neighbourhood crowding indices** (*NCI*'s[36,37]), we assume that the survival of an individual (red square) depends on the proximity of conspecific (red) and heterospecific (blue) neighbours within its neighbourhood of radius r (blue shaded area). The crowding index C_{kf} counts all conspecific individuals j with distances $d_{kj} < r$ of the focal individual k, but weights them by $1/d_{kj}$ (eq. a), assuming that distant neighbours compete less. The crowding index H_{kf} does the same with all heterospecifics (eq. b), and the crowding index I_{kf} weights neighbours of species i additionally by their relative competition strength β_{fi}/β_{ff} (eq. c1), where **β_{fi} is the individual-level interaction coefficient**, which measures the negative impact of one neighbour of species i on survival of individuals of the focal species f. Total crowding $C_{kf} + I_{kf}$ then governs the survival of the focal individual[36] (eq. d).

We find that the **population averages $\overline{C_{kf}}$ and $\overline{I_{kf}}$** of the crowding indices determine the **average survival rate** $\bar{s}_f$ of species f (eq. d; eq. 5 in methods). To incorporate the average survival rate into a model of community dynamics (eq. 7 in methods), we decompose $\overline{C_{kf}}$ and $\overline{H_{kf}}$ into species abundance N_f and measures of spatial patterns (eqs. a, b, c2; eq. 6 in methods). **Conspecific aggregation** k_{ff} describes the extent to which trees of the same species tend to occur in spatial clusters and **heterospecific segregation** k_{fh} describes the extent to which they are separated from heterospecifics. We define our measures k_{ff} and k_{fh} by dividing the average crowding indices $\overline{C_{kf}}$ and $\overline{H_{kf}}$ by their expectation in the absence of spatial patterns[19,25] (eqs. a, b), where c is a scaling factor ($c = 2\,\pi\, r/A$, see methods) and A is the area of the plot.

The emerging quantity B_f (eq. c1) is the **average competition strength of one heterospecific neighbour** relative to that of one conspecific. We compare two scenarios for the individual-level interaction coefficient β_{fi}, one where con- and heterospecifics compete equally ($\beta_{fi}/\beta_{ff} = 1$), and one with phylogenetic similarity as proxy for β_{fi}/β_{ff}, because it is difficult to estimate β_{fi}/β_{ff} for species rich forests in practise[37].

Using data of 720 focal species in 21 large temperate, subtropical and tropical forest plots with sizes of 20 – 50 ha from a global network of forest research plots (CTFS-ForestGEO[6]) (Supplementary Table 1), we find that rare species tend to be more aggregated than common species (Fig. 2, Extended Data Fig. 1). Strikingly,

when fitting the data of each forest plot to a power law[20,27,28], we find that the exponent follows a strong latitudinal gradient (Fig. 2c, Extended Data Fig. 1). Tropical forests show only weak negative correlations between aggregation and abundance (Fig. 1a), but in temperate forests aggregation generally increases strongly with decreasing abundance (Fig. 2b). In contrast to conspecifics, heterospecific segregation was not correlated with abundance (except for some weaker correlations at temperate forests; Extended Data Fig. 2c, d).

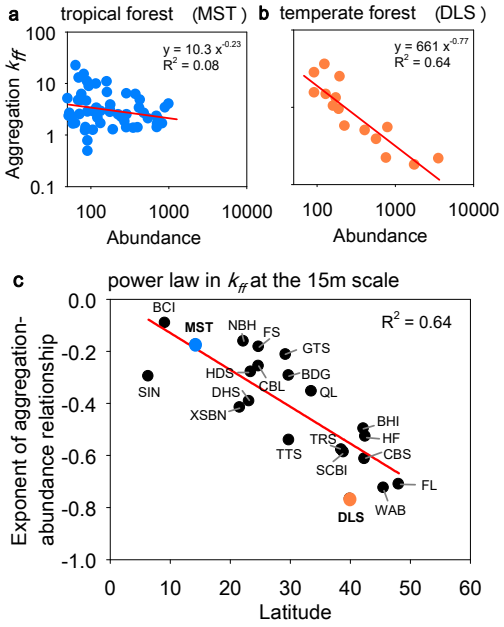

Fig. 2. Latitudinal variation in the scaling of conspecific aggregation with abundance. a, aggregation values for the species in a tropical forest (Mo Singto plot; MST) plotted over their respective abundances (dots) and fitted relationship (line), **b**, same as a), but for a temperate forest (Donglingshan plot; DLS), **c**, latitudinal gradient in the exponent b_f of the aggregation-abundance relationship for the 21 forest plots. Aggregation is defined in Box 1 (eq. a) and is estimated for neighbourhoods of 15 m. We use in our analyses 720 species with at least 50 large trees[19] (diameter at breast height (dbh) ≥ 10 cm. For plot characteristics and acronyms see Supplementary Table 1.

For tropical forests (i.e., low latitudes), our results indicate that mean conspecific neighbourhood tree densities $\overline{C_{kf}}$ increase almost linearly with species abundance (as leaving aggregation k_{ff} constant leads to $\overline{C_{kf}} = c\, k_{ff}\, N_f$; eq. a in Box 1; Fig. 1b). Thus, individuals of rare species will seldom experience the effects of intraspecific competition in this scenario. However, for temperate forests (i.e., higher latitudes), the exponent b_f approaches values of −1, and local conspecific neighbourhood densities are almost independent of abundance (from $\overline{C_{kf}} = c\, k_{ff}\, N_f$ and $k_{ff} = a_f/N_f$ follows $\overline{C_{kf}} = c\, a_f$; eq. a in Box 1; Fig. 1c). Thus, individuals of rare and common species experience similar degrees of conspecific competition in these forests. This counteracts a rare species advantage and as a consequence, existing theory based on invasion analysis can break down[9]. Thus, we find that spatial aggregation of trees is related to species coexistence in important ways, and we need new theories to determine whether and under which circumstances rare species are likely to increase in abundance[9].

The latitudinal gradient in the relationship between conspecific aggregation and abundance (Fig. 1c) and the absence of such a relationship for heterospecifics (Extended Data Fig. 2c) suggest that simple principles may drive the complex spatial structure and dynamics of plant communities across latitudinal gradients. We also found similar latitudinal gradients in the proportion of species showing mostly animal seed dispersal[10], as well as the proportion of species with an arbuscular mycorrhizal (AM) association[13]. Temperate forests are dominated by EM tree species and tropical forests by AM tree species (Extended Data Fig. 3b, c).

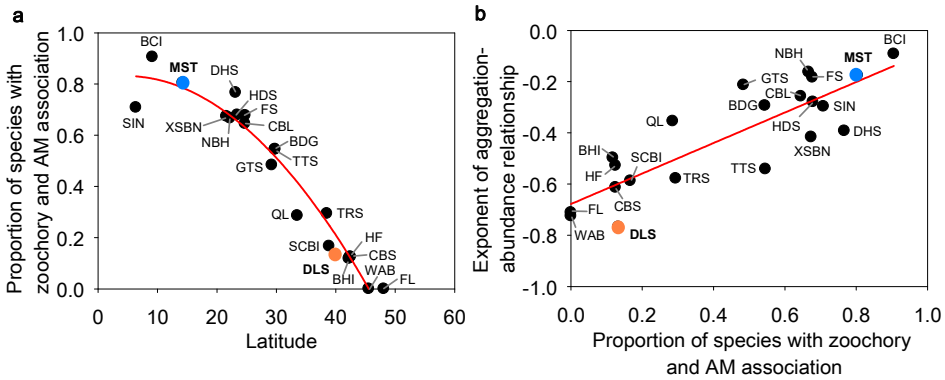

Fig. 3. Latitudinal variation in the proportion of species showing mainly animal seed dispersal and arbuscular mycorrhizal (AM) association. a, latitudinal gradient in the proportion of species per plot that show both, mostly animal seed dispersal and AM association, **b**, relationship between the exponent of the aggregation-abundance relationship and the proportion of species per plot that show mostly animal seed dispersal and AM association for the 21 forest plots. See Extended Data Fig. 3 for the individual relationships with animal seed dispersal and AM association. To outline the overall tendency in the data we fitted in a) a polynomial regression of order 2 and in b) a linear regression. Note that most species showed either arbuscular mycorrhizal (AM) or ectomycorrhizal (EM) associations. Colours indicate the example species of Figure 2.

For the combination of the two traits (i.e., zoochory and AM association), we find an even stronger latitudinal gradient (Fig. 3a), suggesting an explanation of the observed latitudinal gradient in the aggregation-abundance relationship (Fig. 3b). Seed dispersal close to conspecific adults should be advantageous in temperate forests where species-specific EM fungi facilitate conspecific recruitment via root protection[13,39] and counteract negative enemy-driven effects[11,12,13]. In contrast, seed dispersal farther away from conspecific adults should be more advantageous for AM trees, given that an AM association offers less protection from enemies that accumulate near conspecifics than does an EM association[12,39]. In summary, the key mechanism that leads to the different responses of aggregation to abundance is the

way how local clusters emerge with respect to conspecific adults: in tropical forests, mechanisms such as animal seed dispersal lead to emergence of clusters away from adults (Fig. 1a, c), but in temperate forests clusters form close to adults (Fig. 1a, b)[8].

A theory that describes how the observed response of conspecific aggregation to abundance influences species coexistence requires a dynamic population model that relates competition at the population level to the emerging spatial patterns at the scale of individual trees. Here, we derive such an approach[8], which incorporates the critical information on spatial patterns at the scale of individual trees provided by the ForestGEO datasets. We exemplify our theory by a simple model, which assumes that survival of individual trees is reduced in areas of high local tree density, as described by neighbourhood crowding indices[36,37] (Box 1), while reproduction is assumed to be density-independent[7]:

$$\tilde{\lambda}_f(N_{f,t}) = \frac{N_{f,t+\Delta t} - N_{f,t}}{\Delta t}\frac{1}{N_{f,t}} = r_f - (1 - s_f exp(-\beta_{ff} W_f)). \quad (1)$$

Here $N_{f,t}$ is the abundance of the focal species f at time t; the time interval Δt is the 5yr census interval; $\tilde{\lambda}_f(N_{f,t})$ is the per-capita population growth rate (or average individual fitness[40]) of species f as function of species abundance $N_{f,t}$; s_f is a density-independent per-capita background survival rate: r_f the per-capita recruitment rate, and β_{ff} the conspecific individual-level interaction coefficient. W_f, the fitness factor[40], is the average of the sum $C_{kf} + I_{kf}$ of con- and heterospecific neighbourhood crowding taken over all individuals k of species f (Box 1, eq. d) and depends on the abundances of all species, their spatial patterns and the aggregation-abundance relationship (equations 7b, f, 9b).

Our spatially enriched macroscale model can be parameterized with the detailed information on spatial patterns extracted from forest megaplots (see methods). By taking a mean-field approach[41] (i.e., diffuse competition at the community scale[8]) and assuming zero-sum dynamics[2] (due to strong local density dependence), we can decouple the multispecies community model into multiple singe-species models (equation 7), where the multispecies fitness factor W_f of equation 7b is replaced by the single-species fitness factor (equation 7e).

The deterministic invasion criterion[1,5] could be used to assess the consequences of the observed responses of conspecific aggregation to abundance on species coexistence. It asks whether a species will increase in abundance when it invades the resident community at low abundance, but ignores demographic stochasticity[14] and species aggregation[9]. To overcome this limitation, we propose the plot-level extinction risk of species at low abundances as novel stochastic invasion criterion. To this end we translate the resulting single-species macroscale population model (equation 9) into a stochastic birth-death model[42,43] that uses deterministic equations

(equations 12, 13) to describe the dynamics of the probability $P_n(t, N_0)$ that a species with initially N_0 individuals has abundance n at timestep t. In particular, we are interested in the probability of non-successful invasion, given by the probability $P_0(t, N_0)$ that a species starting with a small abundance N_0 is extinct at timestep t. Although the time-dependent extinction probability $P_0(t, N_0)$ of the birth-death model (equations 12, 13) can only be solved in special cases[43], we derived a good approximation for our model (Fig. 4a; Extended Data Figs. 4, 5)

$$P_0(T, x, N_0) = \left[\frac{x}{x+e^{xT}-1}\right]^v \left(\frac{e^{xT}-1}{\frac{e^{xT}}{1-x}-1}\right)^{N_0}, \qquad (2)$$

with $x = \tilde{\lambda}_f(N_s)/r_f$ and $T = r_f t$, where $\tilde{\lambda}_f(N_s)$ is the per-capita population growth rate of species f (equation 9) at a suitable small abundance N_s, r_f the recruitment rate, T the scaled time step, and the parameter v determines the immigration rate (which is $v\, r_f$; equation 12a). Thus, the extinction dynamics of the birth-death model for small initial abundances N_0 approximate that of a linear birth-death model[43] where the birth and death rates (equations 12a, b) are taken at a typical abundance N_s (inset Fig. 4a; Extended Data Figs. 4). This equation provides the desired quantitative link between the extinction risk of a species when rare (i.e., our stochastic invasion criterion) with demographic rates, spatial patterns and immigration of species.

To assess the effects of spatial structure and other non-neutral mechanisms on the invasion success of species when rare, we normalized the extinction risk $P_0(T, N_0)$ by the extinction risk of the corresponding neutral model without immigration (equation 15c). This allows us to quantify the degree of stabilisation, i.e., the factor by which the extinction probability declines due to spatial structure, niche differences and immigration. The scaled per-capita growth rate $\tilde{\lambda}_f(N_s)/r_f$, and thereby stabilisation (Fig. 4c), are determined by the observed species abundance N_f^*, the exponent b_f of the aggregation-abundance relationship, and a risk factor given by $\rho_f = B_f\,(k_{fh}/(k_{ff} - k_{fh}))(J/N_f^*)$ (equation 16). First, stabilisation strongly increases if ρ_f becomes smaller (Fig. 4d), which is the case if niche differences increase (i.e., B_f becomes smaller) and if the average neighbourhoods contain more conspecifics and less heterospecifics (i.e., $k_{fh}/(k_{ff} - k_{fh})$ becomes smaller).

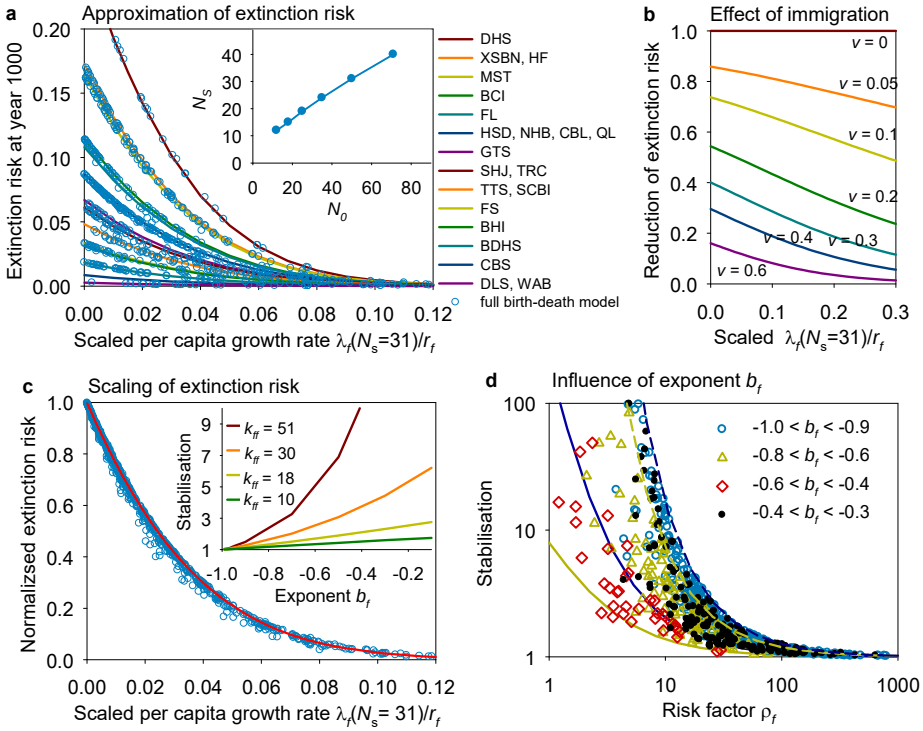

Fig. 4. The stochastic invasion criterion. a, shows the plot-level extinction risk at year 1000 (i.e., t = 200) as a function of the scaled per-capita population growth $\tilde{\lambda}_f(N_s)/r_f$ and for different forest plots. All species start with N_0 = 50 individuals. The lines show the approximation with equation 2 and the open disks are the results of the numerical iteration of the birth-death model for the different species of the 21 forest plots. The inset shows how the fitted typical abundance N_s depends on the initial abundance N_0, **b**, shows how immigration reduces the extinction risk, as given by the first term in equation 2, for a reproduction rate of r_f = 0.1. The constant immigration rate is given by $r_f \upsilon$, and a value of υ = 0.1 means one immigrant every 100 time steps on average. **c**, same as a), but we normalized the extinction probability with that of the corresponding neutral model. The small inset shows how stabilisation (i.e., the invers of the normalised extinction risk) depends for small observed abundances (N_f^* = 50) on aggregation k_{ff} and the exponent b_f of the aggregation-abundance relationship, estimated with equation 2 for parameters k_{fh} = 0.95, J^* = 21000, B_f =1, N_0 = 80, r_f = 0.1, and υ = 0. **d**, Stabilization, the factor by which non-neutral mechanisms reduce the extinction risk, for the 720 species of the 21 forest plots, plotted over the risk factor $\rho_f = B_f(k_{fh}/(k_{ff} - k_{fh}))(J/N_f^*)$ (equation 16c). Different values of the exponent b_f are shown by coloured symbols. Additionally, we show for different typical cases how stabilisation depends on the risk factor ρ_f: the gold lines are for b_f = −0.9 and the blue lines for b_f = −0.3, dashed lines indicate N_f^* = 2000 and solid lines N_f^* = 50. The data in a), c), and d) are from scenario 1 (i.e., no niche differences, N_0 = 50, no immigration).

Second, stabilisation decreases if the exponent b_f approaches values of –1 (i.e., stronger negative correlations between aggregation and abundance) (small inset Fig. 4c). For example, the solid gold line in Fig. 4d represents rare species at temperate forests (N_f^* = 50, b_f = −0.7) and the solid blue line rare species at tropical

forests (N_f^* = 50, b_f = −0.3). Finally, stabilisation increases with increasing abundance N_f^* of the species, which is also included in the risk factor (as shown by comparison of solid versus dashed lines in Fig. 4d).

We find that coexistence in the analysed forest megaplots generally benefits from the emerging spatial patterns (Table 1a). For example, model results for scenarios without niche differences and without immigration indicate that the spatial patterns reduce the 1000-year local extinction risk of invading species for tropical, subtropical and temperate forests on average by factors 1.7, 1.9, and 2.7, respectively, with only moderate declines over longer time periods. Somewhat surprisingly, species at temperate forests tend to show on average higher stabilisation compared to tropical forests (Table 1a).

Table 1. Stabilization (the factor by which the local extinction risk is reduced) by different non-neutral mechanisms through time. We show the effect of combinations of different mechanisms on stabilisation, separately for all species in tropical, subtropical and temperate forests for our 4 scenarios. **a,** scenario 1 (no immigration: υ = 0, no niche differences: $\beta_{fi} = \beta_{ff}$), **b**, scenario 2: (no immigration: υ = 0, niche differences: $\beta_{fi} < \beta_{ff}$), **c,** scenario 3 (immigration with υ =0.1, $\beta_{fi} = \beta_{ff}$), and **d**, scenario 4 (immigration with υ =0.1, $\beta_{fi} < \beta_{ff}$). See Extended Data Fig. 6 for latitudinal gradients in stabilisation and temporal trends.

	1000 years	5000 years	10,000 years	1000 years	5000 years	10,000 years
	a No immigration, no niches			**c Immigration, no niches**		
all	1.91	1.79	1.68	2.62	3.07	3.27
tropical	1.74	1.62	1.51	2.42	2.81	2.96
subtropical	1.93	1.83	1.73	2.62	3.08	3.30
temperate	2.67	2.51	2.39	3.62	4.35	4.85
	b No immigration, but niches			**d Immigration and niches**		
all	2.73	2.46	2.23	3.78	4.34	4.55
tropical	2.58	2.29	2.04	3.63	4.10	4.23
subtropical	2.50	2.32	2.14	3.41	3.99	4.22
temperate	4.44	4.04	3.70	6.03	7.19	7.86

Using expanded model versions, we find that adding niche differences (Table 1b) or a small immigration (υ = 0.1) (Table 1c) lead to further increases in stabilisation, and immigration and niche differences together reduce the plot-level extinction risk in tropical, subtropical and temperate forests by factors 6.0, 7.2, and 7.9, respectively (Table 1d). Finally, larger time periods lead to similar values of stabilisation (Table 1).

Discussion

Developing an approach that integrates observed spatial patterns in forests with multiple ecological processes into mathematical theory is a considerable challenge. Here we present a unified framework integrating spatial point process theory with population models and their corresponding stochastic birth-death models to derive expectations for how interactions between multiple spatial patterns and processes impact stabilisation and species coexistence. The framework relies on spatial patterns that link competition at the scale of individual trees with the dynamics at the population scale. Our theory leads to a closed formula that shows how the extinction risk of species when rare depends on spatial patterns, demographic parameters, and immigration.

Several important ecological insights result from this new theory. First, we have shown that the spatial patterns found in forest megaplots have in general a stabilizing effect under neighbourhood competition[7,8], as they substantially reduce the plot-level extinction risk of a species at low abundances. This result challenges a prevalent perspective[44,45] that spatial patterns alone cannot foster coexistence. However, this assertion arises as a consequence of the assumption of previous spatially-explicit models[7,26,35,44,46] of placing recruits close to their parents, which leads to destabilizing negative aggregation-abundance relationships (with exponents close to −1; inset Fig. 4c) where individuals of rare and abundant species experience similar degrees of conspecific competition (Fig. 1). Our results highlight the critical role that the aggregation-abundance relationship can play in shaping coexistence outcomes. Moving forward we suggest that models studying the forces structuring forest diversity and composition should include a more nuanced representation of seed dispersal[10,47] and its interactions with mycorrhizal associations[11,12,13].

Second, the observed latitudinal gradient suggests stronger stabilizing conspecific negative density dependence in tropical compared to temperate forests[13,22,48] (Extended Data Fig. 7a, b). However, we found a general tendency for forests at lower latitudes to benefit less from the spatial coexistence mechanism (Table 1). This apparent contradiction can be explained by additional factors with opposed latitudinal tendencies that influence the extinction risk in our model (equation 17), such as lower risk factors ρ_f and higher species frequencies at higher latitudes (Extended Data Fig. 8). Nevertheless, species in temperate forests with a low equilibrium abundance (e.g., $N_f^* = 80$) show a substantially lower stabilisation than species at tropical forests (small inset Fig. 4c) and therefore a higher extinction risk. This finding can help to explain why there are fewer rare species in temperate compared to tropical forests.

Third, we found that the frequently used deterministic invasion criterion[1,5] did not yield useful predictions because it was satisfied for nearly all forests analysed here (equation 11) and failed to detect differences in the local extinction risk of species related to demographic stochasticity[14]. Additionally, it does not apply if rare species are more strongly aggregated than abundant species[9], as observed here in temperate forests. This leads to conspecific population-level interaction coefficients that are not constant as commonly assumed[49], but depend negatively on abundance (equation 7c). We have developed new theory that overcomes such issues and allows to determine whether and under what circumstances the abundances of rare species are likely to increase (equations 2, 16). Although we derived our stochastic invasion criterion for a specific population model, we believe that it could also be used for other population models that can be formulated by means of the per-capita growth rate $\tilde{\lambda}_f(N_f)$ (see Supplementary Text).

Our spatial analysis of 21 large forest plots revealed an intriguing latitudinal gradient in the strength of the relationship between conspecific aggregation and abundance that begs for an explanation. Our data (Fig. 3) suggest that the aggregation-abundance relationship arises as an interaction of animal seed dispersal[10] with mycorrhizal associations[11,12,13]. We hypothesize that an ectomycorrhizal (EM) association, as mostly observed in temperate forests, would be beneficial for species with dispersal close to adults (i.e., non-animal seed dispersal) because this allows facilitation of recruitment by ectomycorrhizal (EM) fungi near adults[11,12,13,39]. In contrast, animal seed dispersal farther away from conspecific adults is beneficial because the prevailing AM mycorrhizal associations in tropical forests offer less protection from enemies compared to an EM association[12,39]. Our combined dispersal-mycorrhiza hypothesis therefore provides an extra dimension to the study of negative conspecific density dependence, and an integrated understanding of the interacting effects of both, animal seed dispersal and mycorrhizal associations will be fundamental to our understanding of forces structuring forest diversity and composition.

Overcoming the limitations of macroscale population models, as often used in contemporary coexistence theory[1,4,15,40,50], requires approaches that explicitly consider the lower-level processes that generate the phenomenon of interest[51]. Our results demonstrate the utility of transfer functions that describe the parameters of the macroscale population models, here the population-level interaction coefficients α_{fi} (between species i and f), as a function of individual-level interaction coefficients β_{fi} and measures of the emerging spatial patterns (i.e., k_{ff}, k_{fh}, B_f; equation 7)[8]. Our scaling approach has the decisive advantage that the lower-level parameters of the transfer functions can be parameterized from empirical or experimental knowledge, such as the ForestGEO megaplots[6] in our case. Taking this approach,

we have demonstrated that spatial patterns emerging from individual-level processes play a key role in species coexistence, which underscores the need to understand the mechanisms underlying the spatial heterogeneity of forests in greater detail.

References

1. Chesson, P. Mechanisms of maintenance of species diversity. *Annu. Rev. Ecol. Syst.* **31,** 343–366 (2000).
2. Hubbell, S. P. *The Unified Neutral Theory of Biodiversity and Biogeography*. (Princeton Univ. Press, 2001).
3. Wright, J. S. Plant diversity in tropical forests: a review of mechanisms of species coexistence. *Oecologia* **130,** 1–14 (2002).
4. Kraft, N. J. B., Godoy, O. & Levine, J. M. Plant functional traits and the multidimensional nature of species coexistence. *Proc. Natl Acad. Sci. USA* **112,** 797–802 (2015).
5. Barabás, G., D'Andrea, R. & Stump, S. M. Chesson's coexistence theory. *Ecol. Monogr.* **88,** 277-230 (2018).
6. Davies, S. J. *et al.* ForestGEO: Understanding forest diversity and dynamics through a global observatory network. *Biol. Conserv.* **253**, 108907 (2021).
7. Detto, M. & Muller-Landau, H. C. Stabilization of species coexistence in spatial models through the aggregation–segregation effect generated by local dispersal and nonspecific local interactions. *Theor. Pop. Biol.* **112**, 97–108 (2016).
8. Wiegand, T. *et al.* Consequences of spatial patterns for coexistence in species-rich plant communities. *Nat. Ecol. Evol.* **5**, 965–973 (2021).
9. Ellner, S. P., Snyder, R. E., Adler, P. B. & Hooker, G. Toward a "modern coexistence theory" for the discrete and spatial. *Ecol. Monogr.* **92**, e1548 (2022).
10. Rogers, H.S., Donoso, I., Traveset, A. & Fricke E. C. Cascading Impacts of Seed Disperser Loss on Plant Communities and Ecosystems. *Annu. Rev. Ecol. Evol. Syst.* **52**, 643b–66 (2021).
11. Johnson, D. J., Clay, K. & Phillips, R. P. Mycorrhizal associations and the spatial structure of an old-growth forest community. *Oecologia* **186**, 195–204 (2018).
12. Sasaki, T. *et al.* Role of mycorrhizal associations in tree spatial distribution patterns based on size class in an old-growth forest. *Oecologia* **189**, 971–980 (2019).
13. Delavaux, C. S., *et al.* Mycorrhizal feedbacks influence global forest structure and diversity. *Commun. Biol.* **6**, 1066 (2023).
14. Schreiber, S. J. *et al.* Does deterministic coexistence theory matter in a finite world? *Ecology*, **104**, e3838 (2022).
15. Gibbs T., Levin S. A. & Levine J. M. Coexistence in diverse communities with higher-order interactions. *Proc. Natl Acad. Sci. USA* **119**, e2205063119 (2022).
16. Janzen, D. H. Herbivores and the number of tree species in tropical forests. *Am. Nat.* **104**, 501–528 (1970).
17. Connell, J. H. Diversity in tropical rain forests and coral reefs. *Science* **199**, 1302–1310 (1978).
18. Hubbell, S. P. Tree dispersion, abundance, and diversity in a tropical dry forest. *Science* **203**, 1299–1309 (1979).

19. Condit, R. *et al.* Spatial patterns in the distribution of tropical tree species. *Science* **288**, 143b4–143b8 (2000).
20. Morlon, H. *et al.* A general framework for the distance–decay of similarity in ecological communities. *Ecol. Lett.* **11,** 904–917 (2009).
21. Kalyuzhny, M., Lake, J. K., Wright, S. J. & Ostling A. M. Pervasive within-species spatial repulsion among adult tropical trees. *Science* **381**, 563–568 (2023).
22. LaManna, J. A. et al. Plant diversity increases with the strength of negative density dependence at the global scale. *Science* **356**, 1389–1392 (2017).
23. Seidler, T. G. & Plotkin, J. B. Seed dispersal and spatial pattern in tropical trees. *PLoS Biology* **4**, e344 (2006).
24. McFadden, I. R. *et al.* Disentangling the functional trait correlates of spatial aggregation in tropical forest trees. *Ecology* **100**, e02591 (2019).
25. Wiegand, T. & Moloney, K. A. *A handbook of spatial point pattern analysis in ecology*. (Chapman and Hall/CRC press, 2014).
26. May, F., Wiegand, T. Lehmann, S. & Huth A. Do abundance distributions and species aggregation correctly predict macroecological biodiversity patterns in tropical forests? *Glob. Ecol. Biogeogr.* **25,** 575–585 (2016).
27. Davis, M. A., Curran, C., Tietmeyer, A. & Miller A. Dynamic tree aggregation patterns in a species-poor temperate woodland disturbed by fire. *J Veg Sci.* **16**, 167-174 (2005).
28. Gilbert, S. *et al.* Beyond the tropics: forest structure in a temperate forest mapped plot. *J Veg Sci.* 21, 388–405 (2010).
29. He, F., Legendre, P. & LaFrankie, J.V. Distribution patterns of tree species in a Malaysian tropical rain forest. *J. Veg. Sci.* **8**, 105-114 (1997).
30. Muller-Landau, H. C. *et al.* Interspecific variation in primary seed dispersal in a tropical forest. *J. Ecol.* **96**, 653–667 (2008).
31. Wright, J. S. *et al.* Interspecific associations in seed arrival and seedling recruitment in a Neotropical forest. *Ecology* **97**, 2780–2790 (2016).
32. Chanthorn, W., Getzin, S., Wiegand, T., Brockelman, W. Y. & Nathalang, A. Spatial patterns of local species richness reveal importance of frugivores for tropical forest diversity. *J. Ecol.* **106,** 925–935 (2018)
33. Getzin, S., Wiegand, T., and Hubbell, S. P. Stochastically driven adult-recruit associations of tree species on Barro Colorado Island. *Proc. R. Soc. B* **281**, 20140922 (2014).
34. Usinowicz, J. *et al.* Temporal coexistence mechanisms contribute to the latitudinal gradient in forest diversity. *Nature* **550,** 105–108 (2017).
35. Detto, M. & Muller-Landau, H. C. Rates of formation and dissipation of clumping reveal lagged responses in tropical tree populations. *Ecology* **97**, 1170–118 (2016).
36. Uriarte, M. *et al.* Trait similarity, shared ancestry and the structure of neighbourhood interactions in a subtropical wet forest: implications for community assembly. *Ecol. Lett.* **13,** 1503–1514 (2010).
37. Canham, C. D. *et al.* Neighborhood analyses of canopy tree competition along environmental gradients in New England forests. *Ecol. Appl.* **16**, 540-54 (2006).
38. Lewis, S.L. & Tanner, E.V.J. Effects of above- and belowground competition on growth and survival of rain forest tree seedlings. *Ecology* **81**, 2525–2538 (2000).
39. Bennett, J. A. et al. Plant-soil feedbacks and mycorrhizal type influence temperate forest population dynamics. *Science* **355**, 181–184 (2017).
40. Chesson, P. Scale transition theory: Its aims, motivations and predictions. *Ecol. Complex.* **10,** 52-68 (2012).

41. O'Dwyer, J. & Chisholm, R. A mean field model for competition: From neutral ecology to the Red Queen. *Ecol. Let.* 17: 961–969 (2014).
42. Azaele, S., Pigolotti, S., Banavar J. R. & Maritan, A. Dynamical evolution of ecosystems. *Nature* **444**, 926–928 (2006).
43. Alonso, D. & McKane, A. Extinction dynamics in mainland–island metapopulations: an N-patch stochastic model. *Bull Math Biol.* **64**, 913–958 (2002).
44. Murrell, D. When does local spatial structure hinder competitive coexistence and reverse competitive hierarchies? *Ecology* **91**, 1605–1616 (2010)
45. Chesson, P., & Neuhauser, C. Intraspecific aggregation and species coexistence. *Trends Ecol. Evol.* **17**, 210–211 (2002).
46. Bolker, B. & Pacala, S. W. Spatial moment equations for plant competition: understanding spatial strategies and the advantage of short dispersal. *Am. Nat.* 153, 575–602 (1999).
47. Beckman, N. G. & Sullivan, L. L. The causes and consequences of seed dispersal. *Annu. Rev. Ecol. Evol. Syst.* **54**, 403–427 (2023).
48. Comita, L., Muller-Landau, H. C., Aguilar, S. & Hubbell, S. P. Asymmetric density dependence shapes species abundances in a tropical tree community. *Science* **329**, 330-332 (2010).
49. Broekman, M. J. E., Muller-Landau, H. C., Visser, M. D., Jongejans, E., Wright, S. J., and de Kroon, H. Signs of stabilisation and stable coexistence. *Ecol. Lett.* **22**, 1957–1975 (2019).
50. Serván, C. A., Capitán, J. A., Grilli, J., Morrison, K. E. & Allesina, S. Coexistence of many species in random ecosystems. *Nat. Ecol. Evol.* **2,** 1237–1242 (2018).
51. Loreau, M. *From Populations to Ecosystems*. (Princeton Univ. Press, 2010).

.

Methods

Study areas

Twenty-one large forest dynamics plots of areas between 20 and 50 ha with similar number of tropical, subtropical, and temperate forests were utilized in the present study (Supplementary Table S1). The forest plots are part of the Forest Global Earth Observatory (ForestGEO) network[6] and are located in Asia and the Americas ranging in latitudes from 6.40° N to 48.08° N. Tree species richness among these plots ranges from 36 to 468. All free-standing individuals with diameter at breast height (dbh) ≥1 cm were mapped, size measured, and identified. We focussed our analysis here on individuals with dbh ≥ 10 cm (resulting in 313,434 individuals) and tree species with more than 50 individuals (resulting in initially 737 species). The 10 cm size threshold excludes most of the saplings and enables comparisons with previous spatial analyses. Shrub species were excluded. We also excluded 15 species with low aggregation (i.e., $k_{ff} < k_{fh}$; Box 1), which would lead to negative growth rates at small abundances; ten of them from BCI, two from MST, two from NBH, and one from FS. These (generally less abundant) species are probable relicts of an earlier successional episode when they were more abundant[18,52]. We also excluded the two species *Picea mariana* and *Thuja occidentalis* of the Wabikon forest that are restricted to a patch of successional forest that was logged approximately 40 years ago[53].

Most forest plots (18 of our 21 plots, those with more than one census) allow for estimation of the average mortality risk of individuals with dhh ≥ 10cm within one census period. We estimated mortality across all species and obtained for each forest plot one average mortality rate for trees with dbh ≥10 cm (Supplementary Table 1). In contrast, direct estimation of the per-capita recruitment rate is difficult. We therefore used a shortcut and assumed approximate equilibrium where the unknown per-capita recruitment rate r_f is the same as the known per-capita mortality rate. However, the equation of the local extinction probability (equation 2) we derived for the singe-species model (equation 9) allows for an easy assessment of the effects of species-specific recruitment rates. We also determined for all species used in our analyses the mycorrhizal association types based on available global datasets[54,55,56] and website sources (http://mycorrrhizas.info/infex.html). To determine if a species is mainly dispersed by animals (zoochory) we used the Seed Information Database (https:// data.kew.org/sid) of the Royal Botanic Gardens Kew and available literature[57]. Species without descriptions of mycorrhizal associations and dispersal modes were assigned according to their congeneric species. The proportion of focal species with zoochory, with arbuscular mycorrhizal (AM) association, and with both are shown in Supplementary Table 1.

Proxy for pairwise competition strength between species

Some of our analyses require the ratio β_{fj}/β_{ff} (Box 1) that describes the relative competitive effect[36,58] of individuals of species i on an individual of the focal species f. In general, it is challenging to derive estimates for the pairwise interaction coefficients[37] because this would require unfeasible large data sets to obtain a sufficient number of neighboured f–j species pairs for less abundant species. We therefore compared two scenarios. In scenario 1 we assumed that con- and heterospecific individuals compete equally, thus $\beta_{fj} = \beta_{ff}$. In scenario 2 we assumed that individuals which are close relatives compete more strongly or share more natural enemies than distant relatives[59]. As proxy for this effect, we used phylogenetic distances[60], given in millions of years (MA), as a surrogate for the relative competition strength because they are available for the species in our plots based on molecular data or the Phylomatic informatics tool[61].

For plots without molecular data, we used the V. PhyloMaker2 package[62] to generate a phylogenetic tree for each plot using GBOTB.extented.WP.tre updated from the dated megaphylogeny GBOTB[63] as a backbone. For the other eight plots with molecular data, we followed the method reported by Kress et al.[64] to build the phylogenetic tree based on DNA barcode data. We then used the cophenetic function in the picante package[65] to calculate phylogenetic distance for each plot. In this we assume that functional traits are phylogenetically conserved[36,59,66]. To obtain consistent measures among forest plots, phylogenetic similarities were scaled between 0 and 1, with conspecifics set to 1 and a similarity of 0 was assumed for a phylogenetic distance of 1200 MA, which was somewhat larger than the maximal observed distance (1059 MA). This was necessary to avoid discounting crowding effects from the most distantly related neighbours[59].

Crowding indices for tree competition and measures of spatial patterns

We assume in our example model that survival of a focal tree k is reduced in areas of high local density of con- and heterospecifics (i.e., neighbourhood crowding), e.g., through competition for space, light or nutrients, or natural enemies[16,17,38,67], while reproduction is density-independent with per-capita rate r_f. Analogous models can be derived for crowding effects on the reproductive rate and/or the establishment of offspring (see Supplementary Text). We describe the neighbourhood crowding around tree k of a focal species f by commonly used neighbourhood crowding indices[36,37,58,68,69,70] (*NCI*'s; Box 1), but use separate indices for con- and heterospecific trees.

The conspecific crowding index C_{kf} of a given individual k counts the number of conspecific neighbours j with distances d_{kj} smaller than a given neighbourhood radius r, but weights them by $1/d_{kj}$, assuming that farther away neighbours compete less (equation 3a). The heterospecific crowding index H_{kf} does the same with all heterospecifics (equation 3b), and the interaction crowding index I_{kf} weights heterospecifics additionally by their relative competitive strength β_{fi}/β_{ff} (equation 3c). Thus, we estimate for each individual k three crowding indices

$$\text{conspecific crowding:} \qquad C_{kf} = \sum_{j=1}^{n_f} \frac{1}{d_{kj}} \tag{3a}$$

$$\text{heterospecific crowding:} \qquad H_{kf} = \sum_{i \neq f} \sum_{j=1}^{n_i} \frac{1}{d_{kj}} \tag{3b}$$

$$\text{with niche differences:} \qquad I_{kf} = \sum_{i \neq f} \sum_{j=1}^{n_i} \frac{\beta_{fi}}{\beta_{ff}} \frac{1}{d_{kj}} \tag{3c}$$

where n_i is the number of neighbours of species i within distance r of the focal individual, d_{kj} is the distance between the focal individual k and its jth neighbour of species i, and β_{fi}/β_{ff} is the competitive effect of one individual of species i relative to that of the focal species f [36,37,59,68,69,70].

To link the survival of an individual k to its crowding indices we follow earlier work on individual neighbourhood models[36,37,59,69,70] and assume that the survival rate s_{kf} of a focal tree k of species f is given by

$$s_{kf} = s_f \, exp(- \beta_{ff} (C_{kf} + I_{kf})), \tag{4}$$

where s_f is a density-independent background survival rate of species f and β_{ff} the individual-level conspecific interaction coefficients of species f[36]. Statistical analyses with neighbourhood crowding indices have shown that the performance of trees depends on their neighbours mostly within distances r of up to 10 or 15 m[70], we therefore estimate all measures of spatial neighbourhood patterns with a neighbourhood radius of r = 15 m. We investigate two scenarios, in scenario 1 con- and heterospecifics competing equally at the individual scale (i.e., $\beta_{fi} = \beta_{ff}$), and in scenario 2 the quantity β_{fi}/β_{ff} is proportional to phylogenetic similarity see above "*Proxy for pairwise competition strength between species*").

We use scale transition theory[40] and spatial point process theory[25] to transfer the individual-based microscale information on the number and distance of con- and heterospecific neighbours of focal individuals, which are provided by the ForestGEO census maps, into macroscale models of community dynamics[8]. To this end, we average the survival rates s_{kf} of all individuals k of the focal species f to obtain

the average population-level survival rate $\bar{s}_f$, for which we derived a closed expression for Gamma distributed crowing indices[8]:

$$\bar{s}_f = s_f exp(-\beta_{ff}(\gamma_{ff}\overline{C_{kf}} + \gamma_{f\beta}\overline{I_{kf}})) \quad (5)$$

where $\overline{C_{kf}}$ and $\overline{I_{kf}}$ are the average crowding indices, and the quantities γ_{ff} and $\gamma_{f\beta}$ arise through the averaging because of the non-linearity in equation 4[8], but in our case of high survival rates they are near one and can be neglected (i.e., $\gamma_{ff} \approx 1$ and $\gamma_{f\beta} \approx 1$).

To incorporate the average survival (equation 5) into our population model we need to decompose the average crowding indices into species abundances and measures of spatial patterns (Box 1). Briefly, we do this by expressing the crowding indices in terms of the pair correlation function, a basic summary function of spatial statistics[25], and the mean density $\lambda_f = N_f/A$ of the species f across the whole plot of area A (see equations S1-S8 in Supplementary Text). The resulting measures k_{ff} and k_{fh} of spatial patterns quantify the change in average conspecific and heterospecific neighbourhood crowding, respectively, relative to the case without spatial patterns (i.e., random distribution of the focal species and independent placement of the focal species with respect to the heterospecifics[25]):

$$\overline{C_{kf}} = k_{ff}\,(c\,N_f) \quad (6a)$$

$$\overline{H_{kf}} = k_{fh}\,(c\sum_{i\neq f} N_i) \quad (6b)$$

$$\overline{I_{kf}} = \overline{H_{kf}}\,\frac{\overline{I_{kf}}}{\overline{H_{kf}}} = k_{fh}\,B_f\,(c\sum_{i\neq f} N_i) \approx c\,k_{fh}B_f(J - N_f) \quad (6c)$$

where $c = 2\,\pi\,r/A$ is a scaling factor (see equation S7 in Supplementary Text), A the area of the plot, r the radius of the neighbourhood, J the total number of individuals in the plot, and $B_f = \overline{I_{kf}}/\overline{H_{kf}}$ the average competition strength of one heterospecific neighbour relative to that of one conspecific. The quantity k_{ff} measures spatial patterns in conspecific crowding of species f ($k_{ff} > 1$ indicates aggregation, and $k_{ff} < 1$ regularity), and k_{fh} measures patterns in heterospecific crowding around the focal species f ($k_{fh} < 1$ indicates segregation, and $k_{fh} > 1$ attraction). Note that our measure of conspecific aggregation, which weights neighbours by distance, is correlated to Condit's Omega measure of aggregation[19] that counts the number of neighbours without weighting by distance (Extended Data Fig. 9). Additionally, we found that the strength of the latitudinal gradient was for a radius of say $r > 10$m basically independent of the neighbourhood area over which conspecific aggregation was measured (Extended Data Fig. 2). This was expected because of the distance-weighting (Box 1) where distant neighbours contribute little to total neighbourhood crowding.

Equation (6c) uses two findings of earlier work. First, a crucial insight used in our approach[8] is that crowding competition of individual trees, as described by equation 4, leads in species-rich communities to diffuse competition at the population scale. That is, when taking a mean-field approximation[41,71], the species-specific competition strengths of heterospecifics can be replaced in the macroscale model by the average heterospecific competition strength B_f[8], which summarizes the emerging effects of the individual-level interaction coefficients β_{fi}/β_{ff} at the population-level. For species rich forests at or near a stationary state, B_f is in good approximation a species-specific constant (see Supplementary Text in Wiegand et al.[8]). Second, the strong local density dependence causes approximate zero-sum dynamics, where the total number J of individuals remains constant[2], and the number of heterospecifics is given by $J - N_f$ (equation 6c). Using these approximations in equation 6c decouples the multispecies dynamics and allows us to investigate the dynamics of individual species in good approximation.

In Fig. 2 we fitted for the species of a given forest plot a phenomenological power law where the x-value was the logarithm of abundance N_f and the y-value the corresponding logarithm of k_{ff}[20,27,28]. However, this leads for large abundances to values of k_{ff} close to zero which would indicate strongly regular patterns[25] not found in the data. Instead, in the extreme case without an aggregation mechanism (i.e., random placement of offspring) crowding competition leads to repulsion of conspecifics comparable to segregation k_{fh} of heterospecifics. Thus, to avoid a bias we used the quantity $k_{ff} - k_{fh}$ as the y-value in our fit.

Basic community-level model

Combining equations (1), (5) and (6) leads to the spatially-enriched macroscale model for the per-capita growth rate of species f (also called average individual fitness[40]):

$$\tilde{\lambda}_f(N_{f,t}) = \frac{N_{f,t+1}-N_{f,t}}{\Delta t}\frac{1}{N_{f,t}} = (r_f - 1) + s_f exp(-\beta_{ff} W_f(N_{f,t})), \qquad (7a)$$

where $N_{f,t}$ is the abundance of species f at timestep t, s_f is a density-independent per-capita background survival rate, r_f the per-capita recruitment rate, β_{ff} the individual-level conspecific interaction coefficients of species f, and $W_f(N_{f,t})$ the fitness factor[40] given by

$$W_f(N_f) = c\{k_{ff} N_f + \sum_{i \neq f} B_f k_{fh} N_i\}. \qquad (7b)$$

The community-level interaction coefficients are therefore given by:

$$\alpha_{ff} = c\, \beta_{ff}\, k_{ff} \qquad (7c)$$

$$\alpha_{fh} = c\,\beta_{ff}\,(B_f k_{fh}). \tag{7d}$$

Thus, even if the individual-level interaction coefficients β_{fi} (equations 3a, c) are constant, the community-level conspecific interaction coefficients α_{ff} (equation 7c) are not necessarily constant, as is commonly assumed[49]. Instead, they will depend on abundance if aggregation k_{ff} correlates with abundance[8], as observed in many of our forest dynamics plots (Fig. 2). Assuming approximate zero-sum dynamics we can rewrite the fitness factor to

$$W_f(N_{f,t}) = c\{k_{ff}N_{f,t} + B_f k_{fh}(J - N_{f,t})\}, \tag{7e}$$

and to accommodate the power law in $(k_{ff} - k_{fh})$ we further rewrite the fitness factor to:

$$W_f(N_{f,t}) = c\{(k_{ff} - k_{fh})N_{f,t} + k_{fh}(1 - B_f)\,N_{f,t} + B_f k_{fh} J\}. \tag{7f}$$

Our spatially-enriched macroscale model approximates an underlying individual-based model in the tradition of earlier spatially-explicit work[7,35,45,46,72,73], but uses the empirically observed spatial patterns instead of modelling their dynamics explicitely[8]. To parameterize the model, we used the ForestGEO data sets to determine the values of aggregation k_{ff}, segregation k_{fh}, total community size J, the observed abundance N_f^* of species f, the recruitment rate r_f, and the exponent b_f that describes the scaling of aggregation with abundance (equation 8). In all analyses we set the background survival rate to $s_f = 1$ (i.e., a tree without neighbours within distance r will survive this timestep). To determine the unknown value of β_{ff}, the individual-level conspecific interaction coefficients of species f, we assume that the observed species abundance N_f is close to equilibrium N_f^* and obtain from equation (7a) $\beta_{ff} = -\ln\left(\frac{1-r_f}{s_f}\right)/W_f(N_f^*)$. The influence of uncertainty in the equilibrium abundance N_f^* on our results can be assessed from equations 16 and 17. The effects of large uncertainty (e.g., N_f^* of 50 vs. 2000) is illustrated in Fig. 4d. Note however that the stochastic birth-death model derived from our macroscale model (that considers demographic stochasticity) describes for species with low values of the per-capita growth rate $\tilde{\lambda}_f(N_{f,t})$ non-equilibrium behaviours where the abundances fluctuate (together with aggregation) stochastically.

To consider the observed aggregation-abundance relationships (see Extended Data Fig. 10 for plots) we replace in equation (7f) the quantity $k_{ff} - k_{fh}$ by

$$L(N_{f,t}) = (k_{ff} - k_{fh})\,(N_{f,t} / N_f^*)^{bf}, \tag{8}$$

where N_f^* is the observed species abundance. Thus, $L(N_f^*) = (k_{ff} - k_{fh})$. Note that effects of habitat association or details of dispersal will influence the values of k_{ff}

and cause the observed departures from the aggregation-abundance relationship. With equation (8) we obtain our final spatially enriched model that links the macroscale to the microscale:

$$\frac{N_{f,t+1}-N_{f,t}}{\Delta t}\frac{1}{N_{f,t}} = \tilde{\lambda}_f(N_{f,t}) = (r_f - 1) + s_f\left(\frac{1-r_f}{s_f}\right)^{\frac{W_f(N_{f,t})}{W_f(N_f^*)}} \quad (9a)$$

with

$$W_f(N_{f,t}) = c\left\{(k_{ff} - k_{fh})\left(\frac{N_{f,t}}{N_f^*}\right)^{b_f} N_{f,t} + (1 - B_f)k_{fh}N_{f,t} + B_f k_{fh} J\right\}, \quad (9b)$$

Note that we obtain for the case of $s_f = 1$ (i.e., all mortality depends on neighbourhood crowding) and for small per-capita recruitment rates r_f the approximation

$$\frac{N_{f,t+1}-N_{f,t}}{\Delta t}\frac{1}{N_{f,t}} = \tilde{\lambda}_f(N_{f,t}) = r_f\left(1 - \frac{W_f(N_{f,t})}{W_f(N_f^*)}\right) \quad (9c)$$

which suggests using a scaled mean recruitment rate $\tilde{\lambda}_f(N_{f,t})/r_f$ to remove the effect of the recruitment rate.

The deterministic invasion criterion

Coexistence requires that populations at low abundances N_f increase[1,5], thus $\tilde{\lambda}_f(N_f) > 0$. This is the case if $W_f(N_f)/W_f(N_f^*) < 1$ (equations 9a, c), which leads to:

$$\left(\frac{N_f}{N_f^*}\right)^{b_f+1} < 1 + (1 - B_f)\frac{k_{fh}}{k_{ff}-k_{fh}}\left(1 - \frac{N_f}{N_f^*}\right) < 1 + (1 - B_f)\frac{k_{fh}}{k_{ff}-k_{fh}}, \quad (10)$$

and with $\kappa_f = (1 - B_f)\frac{k_{fh}}{k_{ff}-k_{fh}}$ and $N_f = 1$ we find the deterministic invasion criterion

$$b_f > -1 - \ln(1 + \kappa_f)/\ln(N_f^*) \quad (11a)$$

In the extreme case that con- and heterospecifics competing equally (i.e., $B_f = 1$) we find:

$$b_f > -1, \quad (11b)$$

which is always fulfilled if the exponent $b_f > -1$. In the more realistic case where heterospecifics compete weaker than conspecifics (i.e., $B_f < 1$), equation (11a) indicates that the invasion criterion can be fulfilled even if $b_f < -1$. Indeed, some species of the CBS plot, which shows an exponent of $b_f = -1.077$, fulfil the deterministic invasion criterion due to large values of $k_{fh}/(k_{ff} - k_{fh})$ (and $B_f < 1$; Extended Data Fig. 7e,f). An aggregation-abundance relationship with exponent $b_f < -1$ leads to a type of Allee effect, which reduces the growth rate at low abundances or makes it even negative (Extended Data Fig. 7).

The stochastic invasion criterion

The deterministic invasion criterion ignores the detrimental influence of demographic stochasticity, which can produce a high risk of extinction at small population sizes, even if the per-capita growth rate $\tilde{\lambda}_f$ shows positive values[14]. To be able to consider the impact of demographic stochasticity and immigration, we translate $\tilde{\lambda}_f(N_f)$ into the master-equation framework of a Markov process of birth-death type[42,43], to estimate the probability distribution $P_0(t, N_0)$ that a species with initially N_0 individuals will be extinct at timestep t[74]. A convenient property of the birth-death model is that it uses deterministic equations to describe demographic stochasticity and does therefore not require stochastic simulations to determine extinction probabilities.

The birth-death model describes the dynamics of the probabilities $p_n(t)$ that the population at time t has abundance n. To that end, the model considers the rates b_n and d_n at which reproduction and death events occur. We find from equation (7a) that

$$\text{birth rate:} \qquad b_n = (n + v)\, r_f \tag{12a}$$

$$\text{death rate:} \qquad d_n = n\,[1 - s_f\, exp(-\beta_{ff}\, W_f(n))] \tag{12b}$$

$$d_n = n\, r_f\,, \tag{12c}$$

where the birth rate in equation (12a) includes immigration with a constant rate $v\, r_f$, and equation (12c) gives the death rate of the corresponding neutral birth-death model. Note that we model immigration via a constant rate $v\, r_f$ [42,43,75]. This approach differs from the way immigration is usually modelled in neutral theory[2,26,76].

The birth-death model is given by the differential equation system

$$p_0'(t) = -\, b_0\, p_0(t) + d_1\, p_1(t) \tag{13a}$$

$$p_n'(t) = b_{n-1}\, p_{n-1}(t) - (b_n + d_n)\, p_n(t) + d_{n+1}\, p_{n+1}(t) \qquad \text{for } n \geq 1. \tag{13b}$$

The first equation (13a) shows how the extinction probability $p_0(t)$ changes at time t. It increases if death events occur in populations with abundance $n = 1$ (happening at rate d_1) and decreases if new individuals immigrate to extinct populations (happening at rate $b_0 = v\, r_f$). To obtain the effective change rate of $p_0(t)$, the rates d_1 and b_0 are multiplied with the corresponding probabilities $p_1(t)$ and $p_0(t)$ that the population has one or no individual, respectively. The second equation (equation 13b) keeps track of birth and death events in existent populations. Birth events occur in a population with $n-1$ individuals (which exists with probability $p_{n-1}(t)$) at rate b_{n-1}.

Hence, these events increase the probability $p_n(t)$ of population size n at rate $b_{n-1}p_{n-1}(t)$. Similarly, death events occur in populations of $n+1$ individuals (probability $p_{n+1}(t)$) at rate d_{n+1} and increase $p_n(t)$ at rate $d_{n+1}\,p_{n+1}(t)$. Conversely, for populations with n individuals, both birth and death events (occurring at rates b_n and d_n , respectively) reduce the population probability $p_n(t)$, leading to a reduction of $p_n(t)$ at joint rate $(b_n + d_n)\,p_n(t)$. We solved the system (13a)-(13b) with an implicit integration technique. Details can be found in the supplemental software repository.

For assessment of the invasion criterion we iterated equation (13) in a straightforward way using a small abundance n_0 as initial condition $p_n(t = 0)$. In most of our examples we used a small abundance of $n_0 = 50$, but conducted also analyses for $n_0 = 12$, 18, 25, 36, 50, and 71 (Fig. 4a). We also tested the birth-death model with a symmetric individual-based model (i.e., all species have the same parameters and follow the same rules) described in Wiegand et al.[8] and the Supplementary Text. To this end we used the initial abundance distribution of the individual-based simulations also in the birth-death model. Our test showed that the mean-field approximation works; the birth-death model, parameterized by spatial patterns, was able to correctly predict the species abundance distribution of the individual-based simulations for the same initial conditions and simulation period (Fig. S1 in Supplementary Text).

Given that we are here only interested in the extinction probability $P_0(t, N_0)$ for small initial abundances N_0, we approximate the density-dependent death rate in equation (12b) by a constant d_f, being the death rate $d_f = 1 - e^{-\beta_{ff}W_f(N_s)}$ at a typical low abundance N_s:

$$d_n = n\,d_f \tag{14}$$

Now both, the birth rate b_n (equation 12a) and the death d_n are linear in n and the corresponding master equation (13) can be solved exactly[43]:

$$P_0(t, N_0) = \left[\frac{r_f - d_f}{r_f\,\Delta - d_f}\right]^{\nu} \left(\frac{d_f\,\Delta - d_f}{r_f\,\Delta - d_f}\right)^{N_0}, \tag{15a}$$

where $\Delta = e^{(r_f - d_f)t}$. We note that $r_f - d_f$ is the per-capita growth rate $\tilde{\lambda}_f(N_s)$ at the small abundance N_s. We define $x = \tilde{\lambda}_f(N_s)/r_f = 1 - d_f/r_f$ and $T = r_f t$ being the scaled time. With these definitions we obtain $\Delta = e^{xT}$ and therefore

$$P_0(x, T, N_0) = \left[\frac{x}{x + e^{xT} - 1}\right]^{\nu} \left(\frac{e^{xT} - 1}{\frac{e^{xT}}{1-x} - 1}\right)^{N_0}. \tag{15b}$$

Thus, our approximation of the extinction risk is a function of the per-capita population growth rate at a small abundance divided by the recruitment rate r_f (i.e., the

quantity x), but it depends additionally on the scaled time step $T = r_f\, t$, the initial population size N_0, and the immigration parameter v. The extinction probability of the corresponding neutral model (where $x \to 0$) is given by

$$P_0^n(T, N_0) = \left[\frac{1}{1-T}\right]^v \left(\frac{T}{1+T}\right)^{N_0}. \quad (15c)$$

To apply the approximation of equation 15 to the results of the numerical iteration of the birth-death model (equations 12 and 13), we need to fit (for each value of T and N_0) the value of the small abundance N_s. This can be done in a straightforward way by minimizing e.g., the sum of squares between the extinction risks predicted by the full birth-death model and its approximation for different values of N_s (Extended Data Fig. 4). Thus, the extinction dynamics of the birth-death model for small initial abundances N_0 (and not too large timesteps t) approximates that of a linear birth-death model[43], but with a per-capita growth rate of $\tilde{\lambda}_f(N_s)$ for a typical abundance N_s that is somewhat below the initial abundance N_0 (Fig. 4a). By repeating this exercise for different initial abundances N_0, ranging from 12 to 71, and different time periods of 1000, 5000, and 10000 years, we found still good fits and smooth functions for the best fitting abundance N_s (Fig. 4a; Extended Data Fig. 5)

Link between extinction risk and species properties

The link between the plot-level extinction risk of small populations and the scaled average individual fitness $\tilde{\lambda}_f(N_f)/r_f$ (equation 2) allows us to express the extinction risk as a function of spatial patterns (k_{ff}, k_{fh}, B_f), demographic parameters (r_f, s_f) and the relative abundance of the species (N_f^*/J). We note that the scaled average individual fitness at the typical abundance N_s is approximated by $\tilde{\lambda}_f(N_s)/r_f \approx 1 - W_f(N_s)/W_f(N_f^*)$ (equation 9c). We therefore investigate the ratio $W_f(N_s)/W_f(N_f^*)$ in more detail, it can be expressed as

$$\frac{W_f(N_s)}{W_f(N_f^*)} = \frac{\left(\frac{N_s}{N_f^*}\right)^{b_f+1} + \kappa_f \left(\frac{N_s}{N_f^*}\right) + \rho_f}{1+\kappa_f+\rho_f} \quad (16a)$$

with

$$\kappa_f = (1 - B_f)\frac{k_{fh}}{k_{ff}-k_{fh}} \quad (16b)$$

$$\rho_f = B_f \frac{k_{fh}}{k_{ff}-k_{fh}} \frac{J}{N_f^*} \quad (16c)$$

We can ignore in equation (16a) the quantity κ_f if $B_f(1 + J/N_s) >> 1$, which approximates $B_f >> N_s/J$ for small relative abundances N_s/J of the focal species, and obtain

$$\frac{\tilde{\lambda}_f(N_s)}{r_f} \approx 1 - \frac{W_f(N_s)}{W_f(N_f^*)} = \frac{1-(\frac{N_s}{N_f^*})^{b_f+1}}{1+\rho_f}. \quad (17)$$

Thus, the scaled per-capita growth rate, and the reduction in the plot-scale extinction risk due to non-neutral mechanisms, is mostly driven by a risk factor ρ_f and modified by the term $(N_s/N_f^*)^{bf+1}$ introduced by the abundance-aggregation relationship with exponent b_f. It is therefore instructive to plot the factor by which the extinction risk of the corresponding neutral model is reduced (i.e., stabilisation) in dependence of the risk factor ρ_f to assess the relative impact of abundance N_f^* vs. the exponent b_f of the aggregation-abundance relationship (Fig. 4d). Interestingly, the risk factor ρ_f drops out in the deterministic invasion criterion of equation 10, which indicates that it misses important information.

Scenarios investigated with the birth-death model

We conducted four experiments with the birth-death model to assess the effects of the spatial mechanism of neighbourhood crowding and immigration on the ability of species to persist for 1000 years, 5000 years and 10,000 years when having low abundances (i.e., $N_0 = 50$). Scenarios 1 assumed that con- and heterospecifics compete equally (i.e., no niche differences; $\beta_{fi} = \beta_{ff}$, $B_f = 1$), and scenarios 2 considers niche differences between species approximated by phylogenetic dissimilarity (see above "*Proxy for pairwise competition strength between species*"). Scenarios 3 and 4 are the same as scenarios 1 and 2, but additionally assume a small constant immigration with parameter $\upsilon = 0.1$. For the mean reproduction rate of $r_f = 0.1$ across all plots, this result in an immigration rate of $r_f \upsilon = 0.01$, or 1 immigrant every 100 timesteps. We also conducted analyses of scenario 1 with different initial conditions $N_0 = 12$, 18, 25, 36, 50, and 71 to establish a relationship between N_0 and the abundance N_s (Fig. 4a) that leads to the best fit of the extinction probability $P_0(t, N_0)$ (derived by the numerical iteration of the full birth-death model) by our approximation of equation 2 (Supplementary Data Table 2a).

Additional Method References

52. Flügge, A.J., Olhede, S.C. & Murrell, D.J. The memory of spatial patterns: changes in local abundance and aggregation in a tropical forest. *Ecology* **93**, 1540–1549 (2012).
53. Wang, X. *et al.* Phylogenetic and functional area relationships in two temperate forests. *Ecography* **36**, 883–893 (2013).
54. Soudzilovskaia, N.A.,J. He, S. Rahimlou, K. Abarenkov, M. C.Brundrett, & Tedersoo, L. FungalRoot v.2.0 –An Empirical Database of Plant Mycorrhizal Traits. *N. Phytol.* **235**, 1689–91 (2022).
55. Akhmetzhanova, A.A., *et al.* A rediscovered treasure: mycorrhizal intensity database

for 3000 vascular plant species across the former Soviet Union. *Ecology* **93**, 689–90 (2012).
56. Wang, B., & Y. L. Qiu. Phylogenetic distribution and evolution of mycorrhizas in land plants. *Mycorrhiza* **16**, 299–363 (2006).
57. Jin, J., *et al.* Stronger latitudinal phylogenetic patterns in woody angiosperm assemblages with higher dispersal abilities in China. *J. Biogeogr.* **51**, 269-279 (2024).
58. Fortunel, C. *et al.* Topography and neighborhood crowding can interact to shape species growth and distribution in a diverse Amazonian forest. *Ecology* **99**, 2272–2283 (2018).
59. Fortunel, C., Valencia, R., Wright, S. J., Garwood, N. C. & Kraft, N. J. B. Functional trait differences influence neighbourhood interactions in a hyperdiverse Amazonian forest. *Ecol. Letters* **19,** 1062–70 (2016).
60. Erickson, D. L. *et al.* Comparative evolutionary diversity and phylogenetic structure across multiple forest dynamics plots: a mega-phylogeny approach. *Front. Genet.* **5**, 358 (2014).
61. Webb, C., & Donoghue, M. Phylomatic: tree assembly for applied phylogenetics. *Molecular Ecology Notes* **5**, 181 – 183 (2005).
62. Jin, Y & Qian, H. V.PhyloMaker2: An updated and enlarged R package that can generate very large phylogenies for vascular plants. *Plant Diversity* **44**, 335–339 (2022).
63. Smith, S.A. & Brown, J.W. Constructing a broadly inclusive seed plant phylogeny. *Am. J. Bot.* **105,** 302–314 (2018).
64. Kress, W. J. *et al.* Plant DNA barcodes and a community phylogeny of a tropical forest dynamics plot in Panama. *Proc. Natl Acad. Sci. USA* **106,** 18621–18626 (2009).
65. Kembel, S. W. *et al.* Picante: R tools for integrating phylogenies and ecology. *Bioinformatics* **26**, 1463–1464 (2010).
66. Cadotte, M. W., Davies, T. J. & Peres-Neto, P. R. Why phylogenies do not always predict ecological differences. *Ecol. Monogr.* **87,** 535–551 (2017).
67. Mangan, S. A. et al. Negative plant–soil feedback predicts tree-species relative abundance in a tropical forest. *Nature* **466**, 752–755 (2010).
68. Wiegand, T., *et al.* Spatially explicit metrics of species diversity, functional diversity, and phylogenetic diversity: insights into plant community assembly processes. *Annu. Rev. Ecol. Syst.* **48,** 329–351 (2017).
69. Lasky, J. R., Uriarte, M., Boukili, V. K. & Chazdon, R.L. Trait-mediated assembly processes predict successional changes in community diversity of tropical forests. *Proc. Natl. Acad. Sci. USA* **111**, 5616–21 (2014).
70. Uriarte, M., Condit, R., Canham C. D. & Hubbell, S. P. A spatially explicit model of sapling growth in a tropical forest: does the identity of neighbours matter? *J. Ecol.* **92**, 348–360 (2004).
71. Fung, T. O'Dwyer, J. & Chisholm, R. Effects of temporal environmental stochasticity on species richness: a mechanistic unification spanning weak to strong temporal correlations. *Oikos* e08667 (2022).
72. Bolker, B. & Pacala, S. W. Spatial moment equations for plant competition: understanding spatial strategies and the advantage of short dispersal. *Am. Nat.* **153**, 575–602 (1999).
73. Bolker, B., Pacala, S. W. & Neuhauser, C. Spatial Dynamics in Model Plant Communities: What Do We Really Know? *Am. Nat.* **162**, 135–148 (2003).
74. Grimm, V. & C. Wissel. The intrinsic mean time to extinction: a unifying approach to analysing persistence and viability of populations. *Oikos* **105**, 501–511 (2004).

75. Volkov, I. et al., Density dependence explains tree species abundance and diversity in tropical forests. *Nature* **438**, 658–661 (2005).
76. Chisholm, R. A. & Lichstein, J. W. Linking dispersal, immigration and scale in the neutral theory of biodiversity. *Ecol. Let.* **12**, 1385–1393 (2009).

Acknowledgments

X.W. was supported by the National Key Research and Development Program of China (2022YFF1300501), and the Key Research Program of Frontier Sciences, Chinese Academy of Sciences (Grant ZDBS-LY-DQC019). The Harvard ForestGEO Forest Dynamics plot was funded by the Center for Tropical Forest Science and Smithsonian Institute's Forest Global Earth Observatory (CTFS-ForestGEO), the National Science Foundation's LTER program (DEB 06-20443, DEB 12-37491, and DEB 18-32210) and Harvard University. Thanks to Jason Aylward and Christina McKeown for field supervision, data screening and database management. The FS plot project was supported by the Forestry and Nature Conservation Agency, the Taiwan Forestry Research Institute, and the National Science and Technology Council in Taiwan. Funding for the establishment of the SCBI ForestGEO Large Forest Dynamics Plot was provided by the Smithsonian Global Earth Observatory (SIGEO) initiative, the Smithsonian Institution National Zoological Park, and the HSBC Climate Partnership. The BCI censuses have been made possible through support of the U.S. National Science Foundation (awards 8206992, 8906869, 9405933, 9909947, 0948585 to S.P. Hubbell), the John D. and Catherine D. McArthur Foundation, and the Smithsonian Tropical Research Institute. Funding for the Tyson Research Center (TRC) Forest Dynamics Plot was provided by the National Science Foundation (DEB Awards 1557094 and 2240431 to J.A.M.), the International Center for Advanced Renewable Energy and Sustainability (I-CARES) at Washington University in St. Louis, Tyson Research Center, andForestGEO. We thank the Tyson Research Center staff for providing logistical support. The 25-ha Long-Term Ecological Research Project at Sinharaja World Heritage Site is a collaborative project of the Uva Wellassa University, University of Peradeniya, ForestGEO, with supplementary funding received from the John D. and Catherine T. Macarthur Foundation, the National Institute for Environmental Science, Japan, and the Helmholtz Centre for Environmental Research-UFZ, Germany, for past censuses. The PIs gratefully acknowledge the Forest Department, Uva Wellassa University, and the Post-Graduate Institute of Science at the University of Peradeniya, Sri Lanka for supporting this project. We thank D. Alonso and J. Capitan for discussion of birth-death models and the Kraft lab and R. Condit for valuable feedback on earlier drafts, and numerous local field and lab staff, technicians, interns, volunteers, and researchers for their invaluable

contributions to the collection and management of the forest inventory data.

Author contributions

T.W., X.W., S. F. and A. H. conceived and designed the project, T.W. implemented the models, conducted the simulations, analysed the results, and prepared figures and tables. T. W. and S. F prepared the software. T.W., A.H., S. F., X.W. and N.K. led the writing of the manuscript. X.W. assembled and analysed the plot data and conducted the spatial analyses. All other co-authors contributed data, reviewed, approved, and had the opportunity to comment on the manuscript.

Extended Data Figures

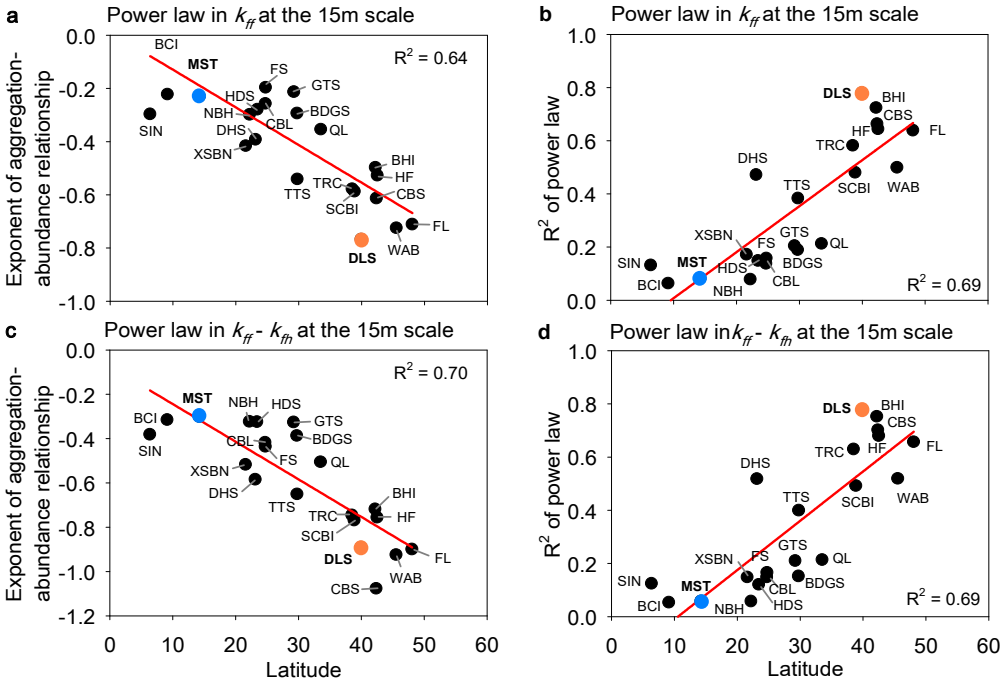

Extended Data Figure 1. Latitudinal gradients in the slope of the abundance-aggregation relationship. a, the power law exponent of the scaling of aggregation k_{ff} with abundance N_f, **b**, the R^2 of the linear regression between ln(k_{fh}) and ln(N_f) for each species, **c**, same as a) but for the scaling of (k_{ff} - k_{fh}) with abundance N_f, **d**, same as b) but for the scaling of (k_{ff} – k_{fh}) with abundance N_f. Our measures of aggregation k_{ff} and segregation k_{fh} are based on neighbourhood crowding indices that count the number of neighbours within distance r of the focal individual, but each neighbour is weighted by the inverse of its distance to the focal individual (Box 1). The neighbourhood distance was in all panels r = 15m. For plot acronyms see Supplementary Table 1. For data see Supplementary Data Table 1. To show the overall tendency we fitted linear regressions.

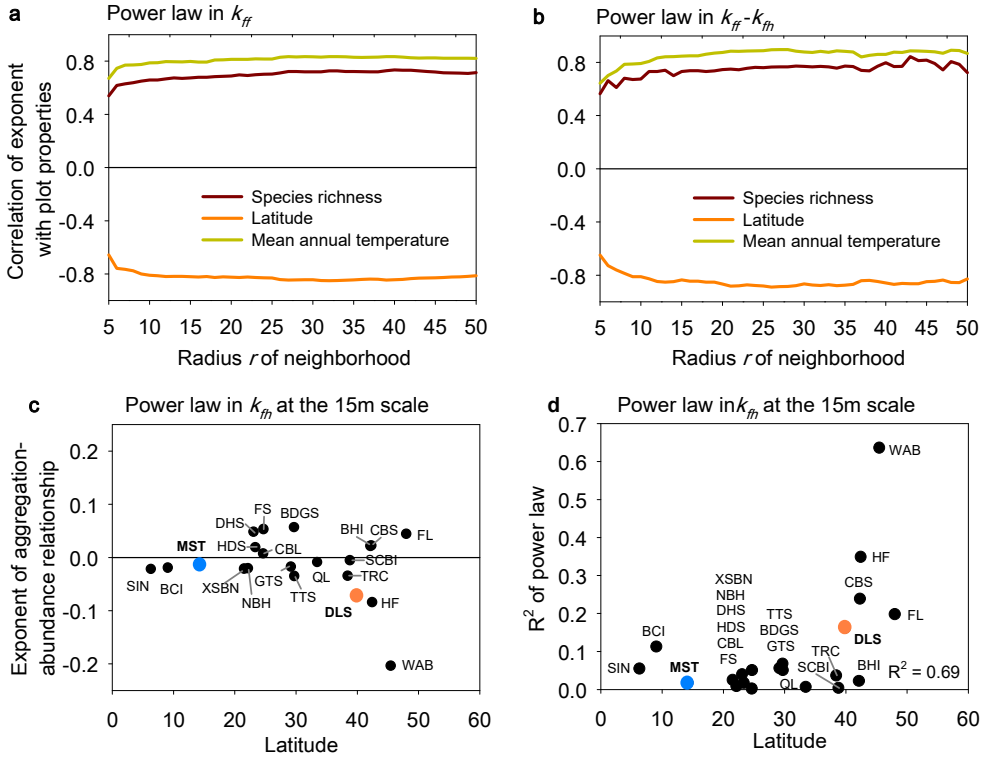

Extended Data Figure 2. Abundance-dependency of aggregation k_{ff} and segregation k_{fh}. **a**, the correlation coefficient between the exponent of the power law and the plot properties species richness, latitude and mean annual temperature for the power law in aggregation k_{ff} with respect to abundance N_f, **b**, the power law in ($k_{ff} - f_{fh}$) with respect to abundance N_f, where k_{ff} is conspecific aggregation and k_{fh} heterospecific segregation, **c**, exponent of the power law of segregation k_{fh} with respect to species abundance N_f for the 21 the ForestGEO data sets, **d**, the R^2 of the linear regression between $\ln(k_{fh})$ and $\ln(N_f)$.

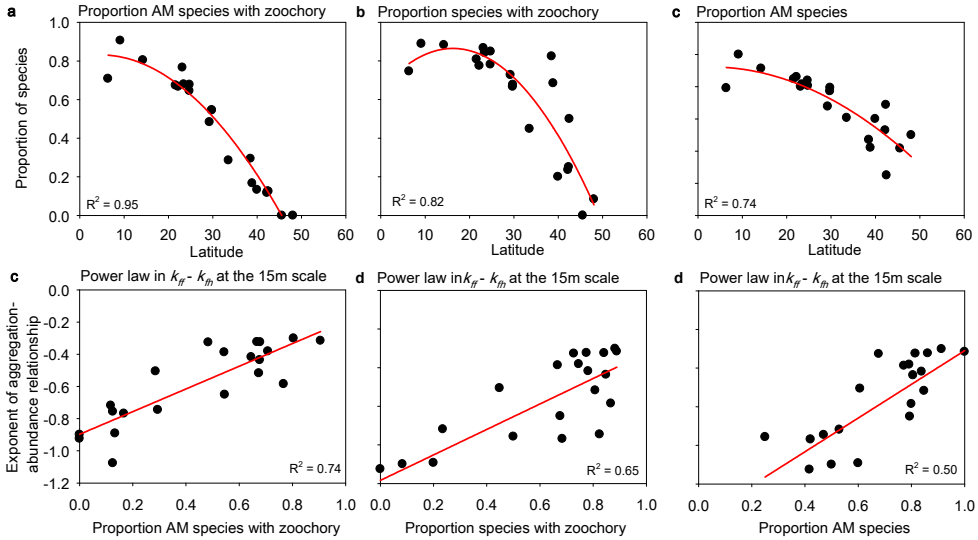

Extended Data Figure 3. Latitudinal variation in the proportion of species showing zoochory and an arbuscular mycorrhizal (AM) association. a, latitudinal gradient in the proportion of species per plot that show both, an AM association and zoochory, **b**, same as a), but only zoochory, **c**, same as a), but only AM species, **d**, relationship between the slope of the aggregation-abundance relationship and the proportion of species per plot that show an AM association and zoochory, **e**, same as d), but only zoochory, **f**, same as d), but only AM species. To outline the overall tendency in the data we fitted in panels a) to c) a polynomial regression of order 2 and in panels d) to f) a linear regression.

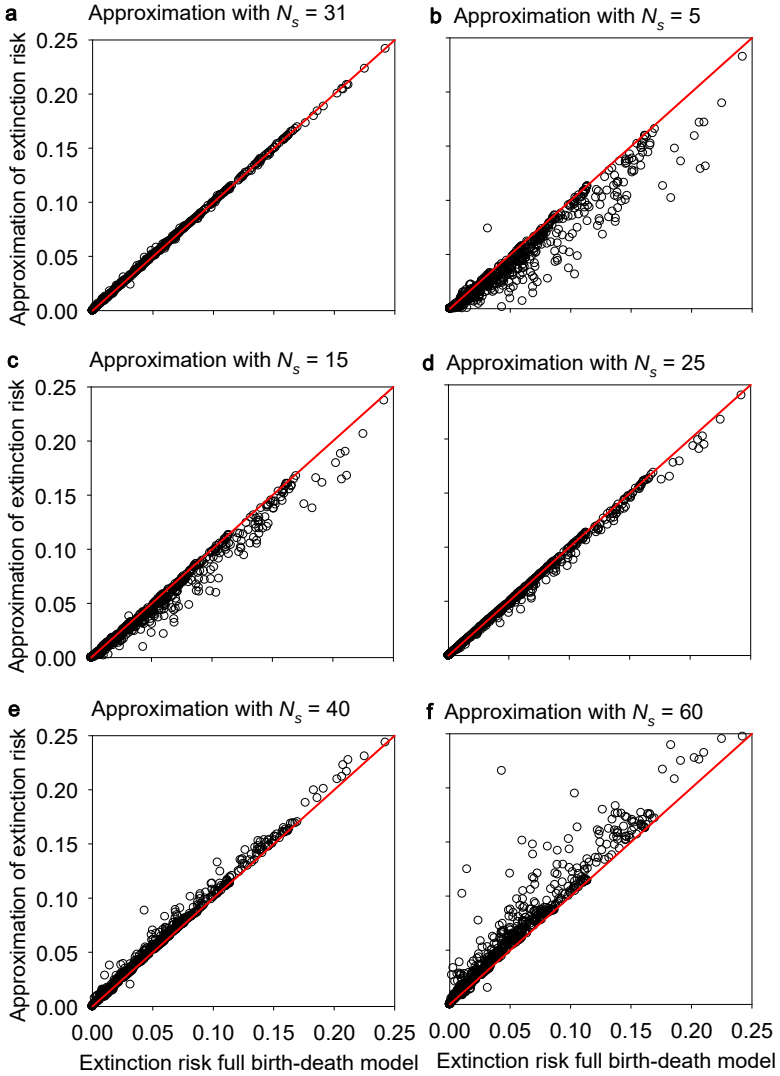

Extended Data Figure 4. Approximation of the extinction probability of the birth-death model. The approximation with equation 2 requires determination of a typical abundance N_s to determine the constant mean population growth rate $\tilde{\lambda}_f(N_s)/r_f$. The different panels show the approximated extinction risk for different values of N_s over the extinction risk determined with the full birth-death model. Panel a) with N_s = 31 shows the best fit. The data are from scenarios 1 (no niche differences, N_0 = 50, no immigration: v = 0), see Supplementary Data Table 1. The red line is the one-to-one line.

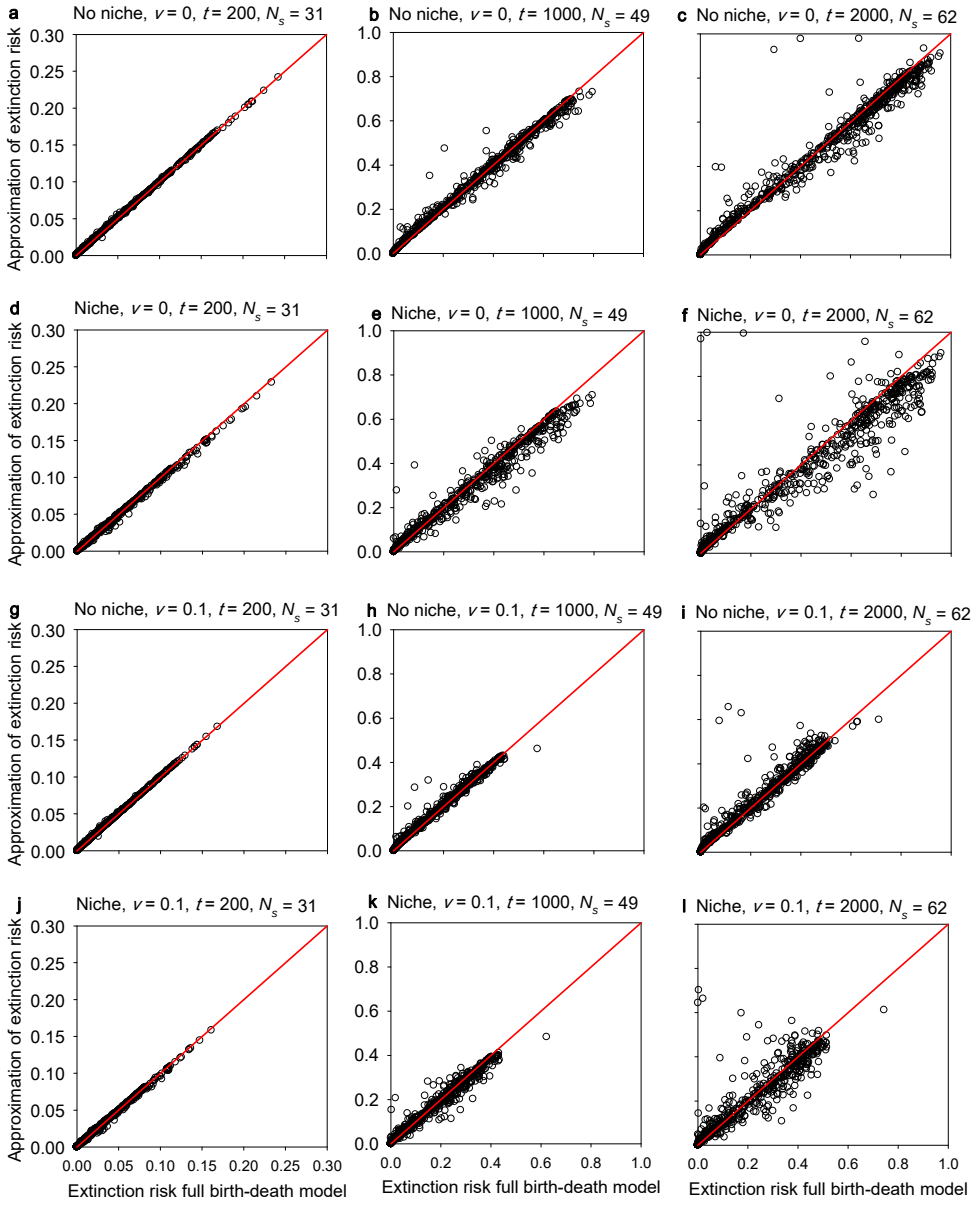

Extended Data Figure 5. Approximation of the extinction probability of the birth-death model for the four scenarios and different time periods. a, – c, scenario 1 (no immigration: $v = 0$, no niche differences: $\beta_{fi} = \beta_{ff}$), **d, – f**, scenario 2: adds niche differences ($v = 0$, $\beta_{fi} < \beta_{ff}$), **g – i**: scenario 3 adds immigration ($v = 0.1$, $\beta_{fi} = \beta_{ff}$), and **g, – i**, scenario 4 adds niche differences and immigration ($v = 0.1$, $\beta_{fi} < \beta_{ff}$). Results are shown for $t = 200$ (1000 years, left), $t = 1000$ (= 5000 years; middle), and $t = 2000$ ($t = 10{,}000$ years; right). The red line is the one-to-one line.

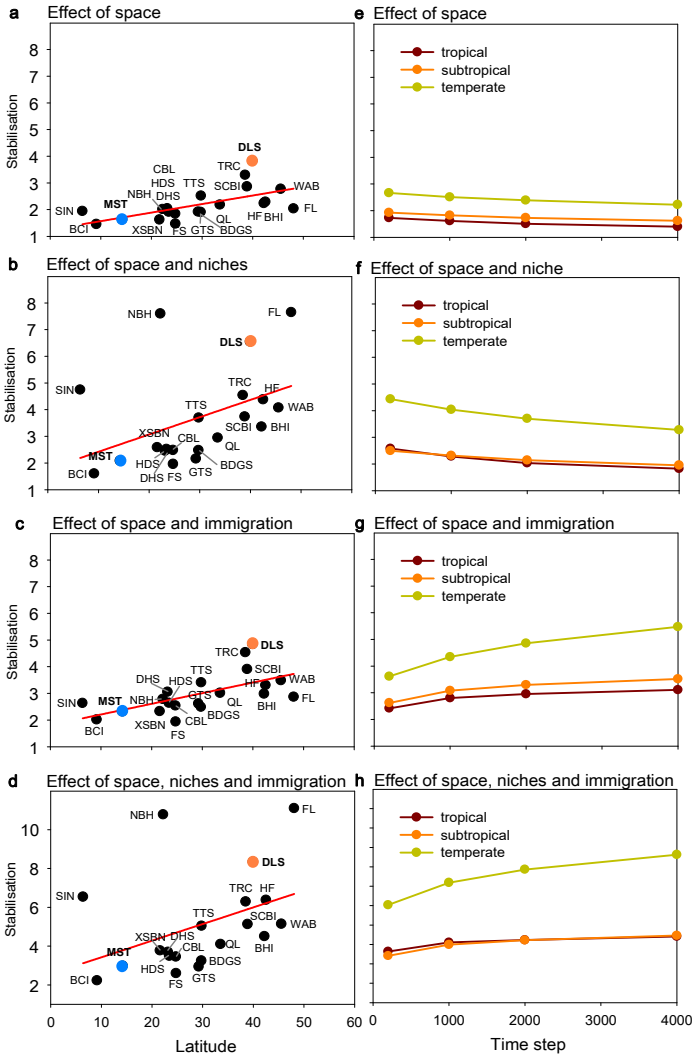

Extended Data Figure 6. Stabilization (the factor by which the extinction risk is reduced) by different non-neutral mechanisms through time. Latitudinal variation in the reduction $P_0(t,N_0)/P_0^n(t,N_0)$ of the extinction risk, as influenced by spatial structure, niche differences and immigration. **a,** mean stabilisation at year 1000, per forest plot for scenario 1 (no immigration: $\upsilon = 0$, no niche differences: $\beta_{fi} = \beta_{ff}$) that represents the effect of spatial structure, **b**, same as a, but for scenario 2 that adds niche differences ($\upsilon = 0$, $\beta_{fi} < \beta_{ff}$), **c**, same as a, but for scenario 3 adds immigration to scenario 1 (υ =0.1, $\beta_{fi} = \beta_{ff}$), **d**, scenario 4 adds niche differences and immigration (υ =0.1, $\beta_{fi} < \beta_{ff}$). **e** – **h**: Changes in stabilisation through time, separately for tropical, subtropical and temperate forests. **e**, scenario 1, **f**, scenario 2, **g**, scenario 3, and **h**, scenario 4. The initial abundance was N_0 = 50 individuals. In scenarios with niche differences we assumed that more closely related species competed more strongly. The birth-death models were parameterized for 720 species of the 21 ForestGEO plots. We excluded the temperate forest at CBS because the exponent $b_f < -1$ (Extended Data Fig. 1C) produced an extinction risk higher than the neutral model. To outline the overall tendency in the data we fitted in panels a) to d) a linear regression to the data.

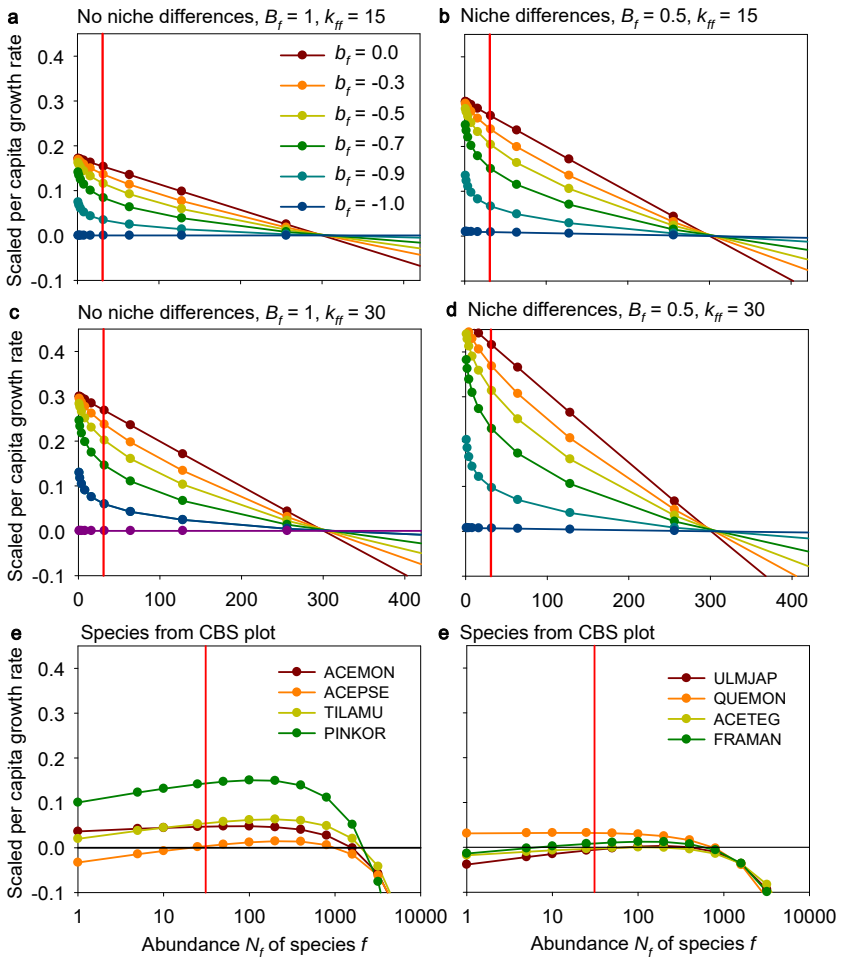

Extended Data Figure 7. Dependency of the per capita population growth rate on the exponent of the aggregation-abundance relationship. a, Examples for the influence of the exponent b_f on the per capita population growth rate for typical parameters N_f^* = 300, N_s = 31, J = 20,000, r_f = 0.1, k_{ff} = 15, k_{fh} = 0.96, B_f = 1 and c = 0.000189. **b**, same as a, but for niche differences (B_f = 0.5). **c,** and **d,** same as a) and b), but larger aggregation (i.e., k_{ff} = 30). **e,** and **f**, examples for the CBS plot for scenario 2 with niche differences (i.e., B_f < 1). We assumed that individuals compete at the individual scale more strongly if they phylogenetically more similarity. The CBS plot shows a power law exponent of b_f = −1.077, which leads to unstable dynamics if con- and heterospecifics compete equally at the individual scale. However, niche differences allow a few species (*Acer mono* (ACEMON), *Tilia amurensis* (TILAMU), *Pinus koraiensis* (PINKOR), *Ulmus japonica* (ULMJAP), *Quercus mongolica* (QUEMON)) to fulfil the deterministic invasion criterion (equation 11a). They are all abundant species that show weak aggregation. The vertical red lines indicates the value of the average individual fitness (at N_s = 31) that determines the extinction risk of a population with initially 50 individuals after 1000 years.

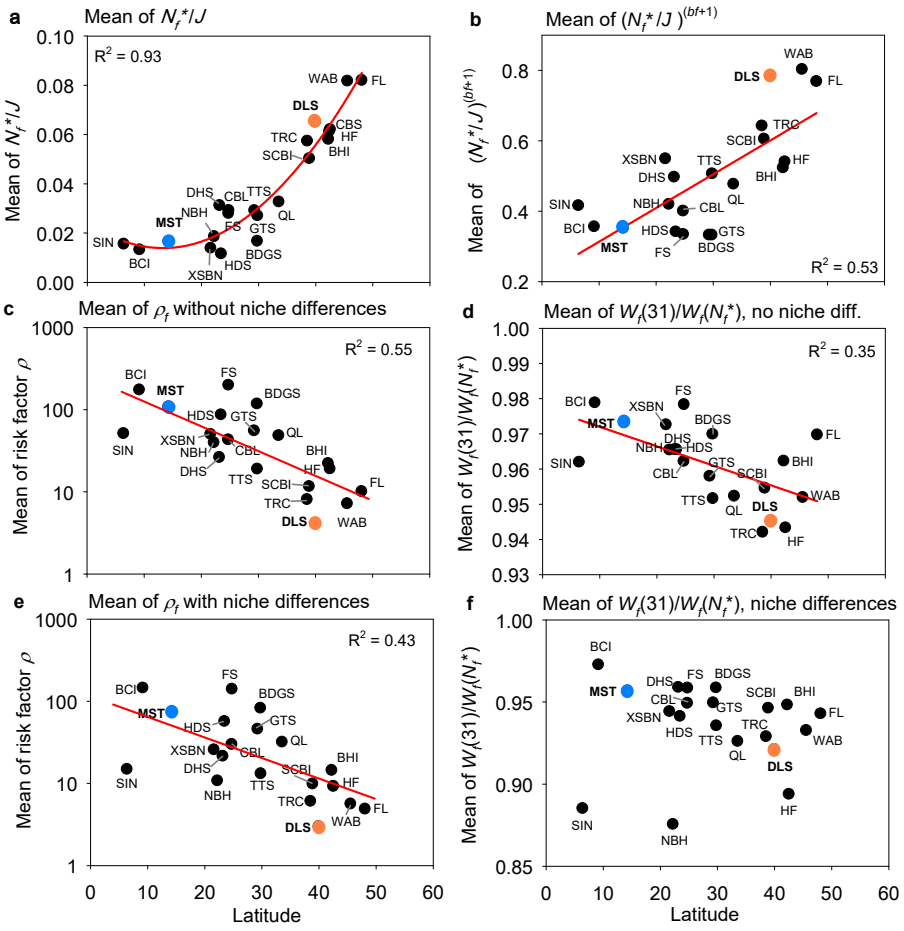

Extended Data Figure 8. Which properties of a species lead to a low extinction risk? The panels show different quantities that drive the average population growth $\tilde{\lambda}_f(N_s)$ at the best fitting typical abundance N_s, which determines the extinction risk (equation 17). **a**, the mean relative abundance N_f^*/J, which drives the risk factor ρ_f, averaged over all species of a given plot shown in dependence on latitude, **b**, same as a), but $(N_f^*/J)^{(bf-1)}$ as it appears in equation 16a, **c**, the mean of the risk factor ρ_f taken over all focal species in each plot, in dependence on latitude, **d**, the mean of the ratio $W_f(N_s)/W_f(N_f^*)$ for N_s = 31 (eq. 16a) that drives the average individual fitness (eqs. 9a, 17) and thereby the extinction risk (equation 2), **e**, same as c), but for niche differences, **f**, same as d), but for niche differences. To outline the overall tendency in the data we fitted in panels a) a polynomial regression of order 2 and in panels b) and d) a linear regression, and in panels c) and e) an exponential regression.

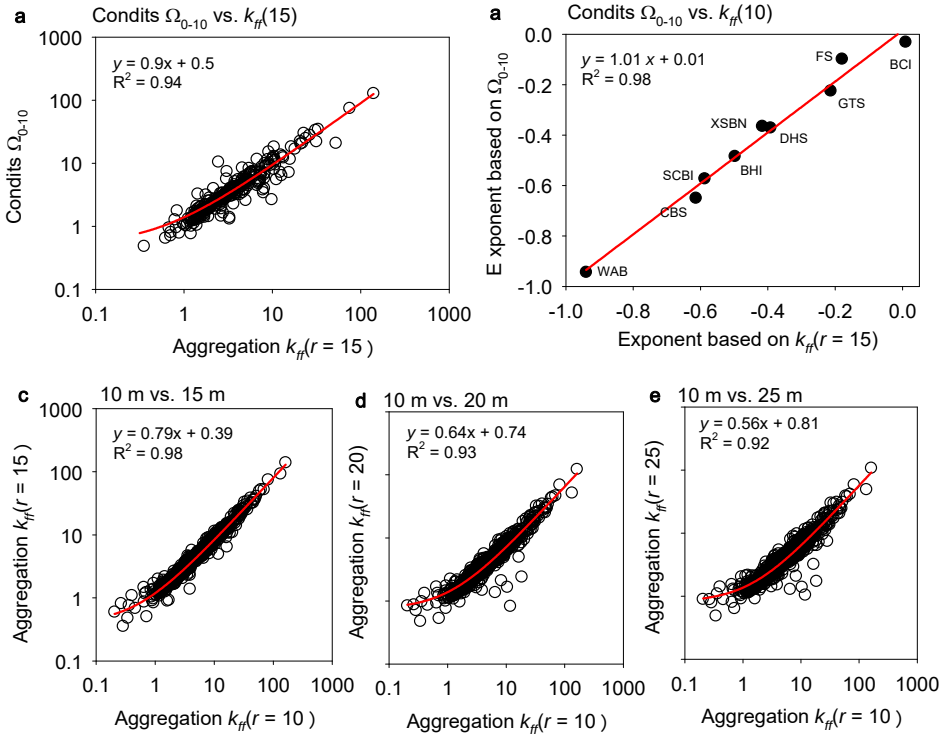

Extended Data Figure 9. Sensitivity of the aggregation-abundance relationships to the measure of aggregation. **a**, Condits's $\Omega_{1\text{-}10}$ aggregation measure for the species analysed in Wiegand et al. (2021) plotted over the corresponding values of the distance-weighted aggregation measure $k_{ff}(r = 15)$ used in the present study, **b**, exponents of the aggregation-abundance power-law derived with Condits's $\Omega_{1\text{-}10}$ plotte over the corresponding values of the distance-weighted aggregation measure $k_{ff}(r = 15)$, **c**, comparison of the distance-weighted aggregation measure $k_{ff}(r)$ for different neighborhood radii 10m vs. 15m, **d**, comparison of the distance-weighted aggregation measure $k_{ff}(r)$ for different neighborhood radii 10m vs. 20m, **e**, comparison of the distance-weighted aggregation measure $k_{ff}(r)$ for different neighborhood radii 10m vs. 25m. To outline the overall tendency in the data we fitted linear regressions to the data.

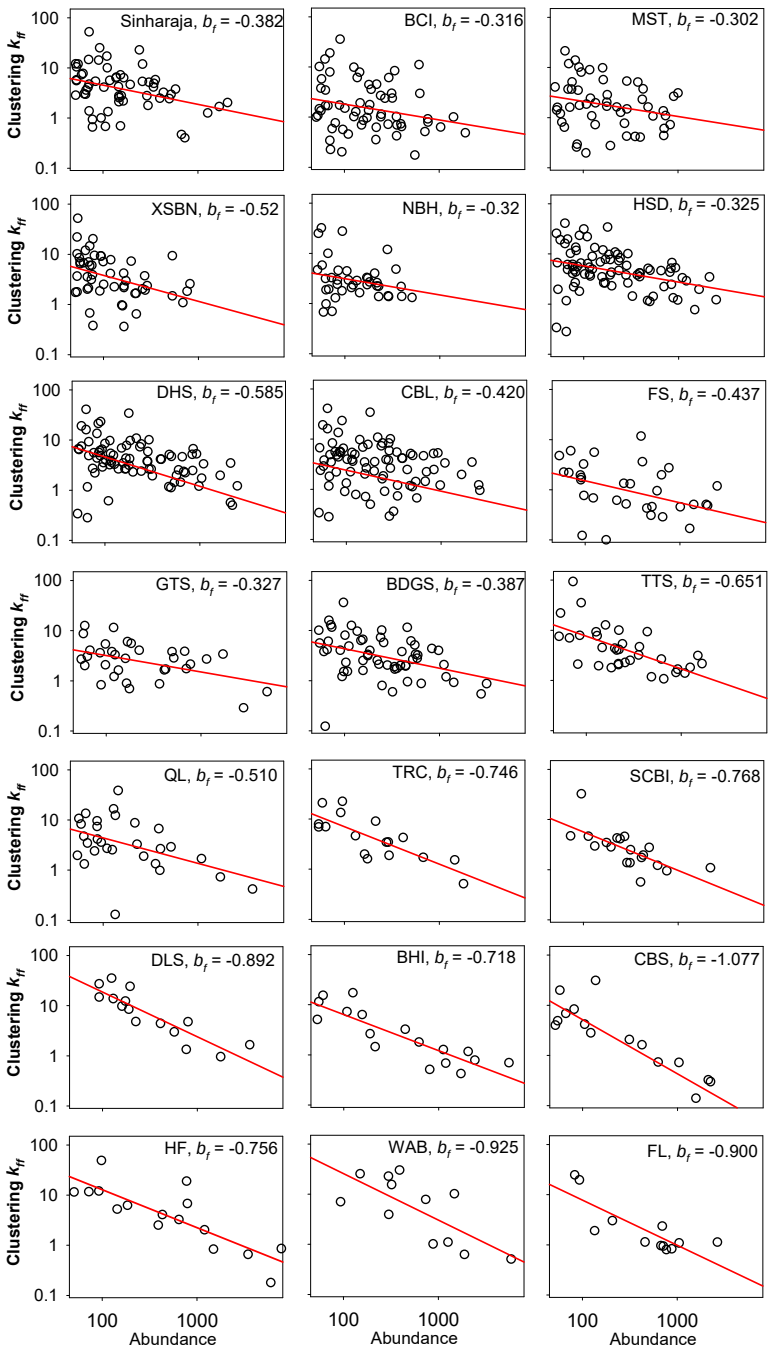

Extended Data Figure 10. Aggregation – abundance relationships for the 21 Forest-GEO plots. The panels show the relationships between corrected aggregation $L(N_f)=(k_{ff} - k_{fh})$ (y-axis) and abundance N_f (x-axis) (equation 8). The value of b_f is the slope of the power law $L(N_f) = a_f N_f^{bf}$ (red line), estimated by linear regression analysis of $\log(k_{ff} - k_{fh})$ over $\log(N_f)$. We used for the analysis focal species f with more than 50 individual. For plot acronyms see Supplementary Table 1.

Supplementary Table 1: Characteristics of the selected forest plots.

Plot	Acronym	Latitude	Elevation	Forest type†	No. species	Individuals ≥10cm dbh	Species ≥10cm dbh	Focal species‡	Area (ha)	Mortality rate††	Prop. zoochory§	Prop. AM$	Prop. AM + zoochory§$
Sinharaja	SHJ	6.40	500	trop.	239	17070	167	59	25	0.087	0.75	0.79	0.71
BCI	BCI	9.15	140	trop.	304	20647	238	63 (-10)	50	0.113	0.89	1.00	0.91
MoSingto	MST	14.26	770	trop.	262	15665	214	52 (-2)	30	0.136	0.88	0.91	0.80
Xishuangbanna*	XSBN	21.61	789	trop.	468	12263	339	52	20	0.14	0.81	0.85	0.67
Nabanhe	NBH	22.23	932	trop.	290	8512	221	40 (-2)	20	-	0.78	0.86	0.67
Heishiding	HSD	23.45	567	trop-subtr.	245	30992	148	82	50	0.1	0.84	0.81	0.68
Dinghushan*	DHS	23.16	350	subtr.	210	11906	131	30	20	- 0.18	0.87	0.80	0.77
Chebaling	CBL	24.72	495	subtr.	228	10159	148	32	20	-	0.78	0.84	0.65
Fushan*	FS	24.76	667	subtr.	110	19261	77	33 (-1)	25	0.071	0.85	0.81	0.68
Gutianshan*	GTS	29.25	581	subtr.	159	18215	109	33	24	0.09	0.73	0.68	0.48
Badagongshan	BDGS	29.77	1406	subtr.	232	25121	186	57	25	0.06	0.67	0.77	0.54
Tiantong	TTS	29.81	454	subtr.	154	14967	107	34	20	0.08	0.68	0.79	0.55
Qinling*	QL	33.54	1431	temp.-subtr.	121	11698	84	29	25	-	0.45	0.61	0.29
Tyson Research Center	TRC	38.52	203	temp.	46	6520	38	17	20	0.085	0.82	0.47	0.29
SCBI	SCBI	38.89	330	temp.	65	8165	49	19	25	0.08	0.68	0.42	0.17
Donglingshan	DLS	39.96	1400	temp.	51	9558	39	15	20	0.04	0.20	0.60	0.13
Baihua*	BHI	42.22	793	temp.	63	17197	34	17	24	0.07	0.24	0.53	0.12
Changbaishan*	CBS	42.38	801	temp.	52	9995	34	16	25	0.05	0.25	0.69	0.13
Harvard Forest	HF	42.54	354	temp.	55	23901	34	16	35	0.14	0.50	0.25	0.13
Wabikon*	WAB	45.55	501	temp.	36	14021	22	12 (-2)	25.2	0.04	0.00	0.42	0.00
Fenglin	FL	48.08	447	temp.	46	8601	23	12	30	0.11	0.08	0.50	0.00

* Bar code phylogeny, genus level phylogenies were used for all othert plots; † trop.: tropical forests, subtr.: subtropical forests, temp.: temperate forests; ‡ The numbers give the number of focal species with at least 50 individuals with dbh >= 10cm, we excluded species with $k_{ff} < k_{fh}$ (the numbers in parenthesis) and two species at the Wabikon forest located in a patch of successional forest that was logged approximately 40 yr ago; †† The average mortality rate for trees with dbh > 10 cm in the plot. Assuming approximate equilibrium, we used the values of the mortality rate to parameterize the unknown per capita recruitment rates r_f. We used a recruitment rate of 0.1 for the 3 plots without mortality data. The mortality rate of the TRC plot was estimated from a 13.4 ha section of the 20 ha plot; § Proportion of species showing mostly animal seed dispersal; $ Proportion of species with arbuscular mycorrhizal association.

Supplementary Table 2: Explanation of important mathematical symbols

Symbol	Meaning
(A) Population level quantities	
$N_{f,t}$, N^*_f	abundance of species f at time t and corresponding observed abundance.
$J = \sum_i^S N_i^*$	total community size in equilibrium (eq. 6c).
Δt	time step, in our case 5 years, the census interval of the ForestGEO plots.
r_f	average number of offspring of an individual of species f within the 5 year census interval. Turnover if species is close to equilibrium (eq. 1).
s_f	background per capita survival rate of species f in absence of neighbourhood competition within the 5 year census interval (eq. 1).
$\bar{s}_f$	the average population-level survival rate of focal species f (eq. 5)
β_{ff}	conspecific individual-level interaction coefficient of the focal species f. Defines the strength of negative density dependence (eq. 1).
β_{fi}	individual-level interaction coefficient, measures the negative impact an individual of species i has on the survival of individuals of the focal species f.
β_{fi}/β_{ff}	relative individual-level interaction coefficient, ranges between zero and one. We use phylogenetic similarity as surrogate for β_{fi}/β_{ff}. Large similarity (i.e., $\beta_{fi}/\beta_{ff} \approx 1$ leads to strong competition whereas low similarity ($\beta_{fi}/\beta_{ff} << 1$) leads to weak competition (eq. 3c).
A	area of the observation window.
f	focal species.
b_f	exponent of the aggregation-abundance power law (eq. 8).
$\tilde{\lambda}_f(N_{f,t})$	average individual fitness of species f, a key quantity that can be derived from the macroscale model (eq. 1, 9). Also called per capita population growth rate.
$W_f(N_{f,t})$	the fitness factor of species f, in our case the average of the neighbourhood crowding indices $NCI_k = C_{kf} + I_{kf}$ of the individuals k of species f (eq. 7).
(B) quantities for neighbourhood crowding indices	
r	neighbourhood radius: all individuals within distance r of a focal individual are counted, we use r = 15m.
k	the focal individual (eq. 3, Box 1).
NCI_k	the neighbourhood crowding index of individual k, it counts the number of individuals within the neighbourhood radius r of individual k, but weights each neighbour

	by the inverse of its distance to individual k. We decompose NCI_k into separate indices for con- and heterospecific neighbours: $NCI_k = C_{kf} + I_{kf}$
C_{kf}	conspecific crowding index: distance-weighted number of conspecific neighbours within distance r of individual k of the focal species f (eq. a in Box 1)
H_{kf}	heterospecific crowding index: distance-weighted number of heterospecific neighbours within distance r of individual k of the focal species f (eq. b in Box 1)
I_{kf}	heterospecific interaction crowding index: number of conspecific neighbours within distance r of individual k of the focal species f, weighted by distance and relative individual-level interaction coefficient β_{fi}/β_{ff} (eq. c2 in Box 1)
$\overline{C_{kf}}$	the average conspecific crowding index of species f, can be decomposed into measures of spatial patterns and abundances (eq. 6a). As edge correction we used only individuals for averaging that had complete neighbourhoods with radius r within the plot.
$\overline{H_{kf}}$	the average heterospecific crowding index of species f, can be decomposed into measures of spatial patterns and abundances (eq. 6b). Same edge correction as for $\overline{C_{kf}}$.
$\overline{I_{kf}}$	the average heterospecific interaction crowding index of species f, can be decomposed into measures of spatial patterns and abundances (eq. 6c). Same edge correction as for $\overline{C_{kf}}$.
$c = 2\pi\, r/A$	scales population sizes from the plot scale with area A to the neighbourhood scale with area $\pi\, r^2$. The circumference of the neighbourhood is used because each neighbour is weighted by the inverse of its distance to the focal individual (see Supplementary Text, eq. S4).

(C) point pattern quantities

k_{ff}	an index of conspecific aggregation of the focal species f. It is the mean conspecific crowding index C_{kf} (eq. 6a), divided by the mean density of the species across the whole plot. Thus, $k_{ff} > 1$: clustering, $k_{ff} \approx 1$: random pattern, and for $k_{ff} < 1$: regularity.
k_{fh}	an index of segregation or attraction of heterospecifics to the focal species f. It is the mean heterospecific crowding index H_{kf} (eq. 6b), divided by the mean density of heterospecifics across the whole plot. Thus, $k_{fh} > 1$: attraction (more than expected heterospecific neighbours), $k_{fh} \approx 1$: independence, and $k_{fh} < 1$: segregation (fewer than expected heterospecific neighbours).
B_f	describes the effect of niche differences, it is $\overline{I_{kf}}/\overline{H_{kf}}$, the average (relative) heterospecific neighbourhood competition strength suffered by the typical individual of species f from one heterospecific individual within its neighbourhood with radius r

	(eqn. 6c, Box 1). It indicates how much the competition strength of one heterospecific neighbour differs on average from that of one conspecific neighbour. For $B_f = 1$ con- and heterospecifics compete equally at the local neighbourhood scale.
$L(N_f)$	the corrected power law relationship between aggregation and abundance (eq. 8), which yields at the observed abundance N_f^* the observed value of $k_{ff} - k_{fh}$.
b_f	exponent of the aggregation-abundance power law (eq. 8).
κ_f	a quantity appearing in the invasion criteria (eq. 11a, 16a,b).
ρ_f	the risk factor, which appearing in the extended invasion criteria (eq. 16c), it dominates the ratio $W_f(N_f)/W_f(N^*_f)$ of the fitness functions (eq. 9) and is positively related to the extinction risk (Figure 4d).

(D) variables of the birth-death model

$P_n(t)$	the probability of population size n at timestep t.
n	population size.
b_n	the birth rate (eq. 12a).
d_n	the death rate (eq. 12b).
v	parameter determining the immigration rate, which is given by $r_f v$ (eq. 12a).
N_0	initial abundance in the birth-death model.
$P_0(t, N_0)$	the probability that a species with initially N_0 individuals will be extinct at time step t (eqs. 2, 15a,b; Fig. 4a)
$P_0^n(t, N_0)$	the extinction probability of the corresponding neutral model with reproduction rate r_f (eq. 15c).
$P_0(t, N_0 / P_0^n(t, N_0)$	reduction in the extinction probability relative to that of the corresponding neutral model (with $\tilde{\lambda}_f(N_f) = 0$) for all abundances N_f), the effects of non-neutral mechanisms (here neighbourhood crowding) on the ability of species to persist when at low abundances.
N_s	The birth-death process starting with a low abundance N_0 can be approximated by a linear birth-death process, using the per capita population growth rate $\tilde{\lambda}_f(N_s)$ at a typical small abundance N_s. The value of N_s can be determined, for a given initial condition N_0 and time frame t, by comparing the result of the numerical iteration of the birth-death model with the corresponding results of equation (2) (Extended Data Figs. 4).
d_f	per capita death rate at a typical low abundance N_s, being $d_f = 1 - e^{-\beta_{ff} W_f(N_s)}$

Supplementary Text

Studies investigating the aggregation-abundance relationship

We list here studies that related aggregation in the spirit of Condit et al. (2000) to abundance, they generally found that Condit's Ω increased with decreasing abundance. Unfortunately, most of these studies showed graphs that correlated Ω or SES(Ω) (but not ln Ω) with ln(abundance), but often for several size classes together.

Condit, R. *et al.* Spatial patterns in the distribution of tropical tree species. *Science* **288**, 1414–1418 (2000). Log(Ω_{0-10}) values were plotted against Log(abundance) (Fig. 4), data of Table 2 for six tropical forests (Pasoh, BCI, Mudumalai, Sinharaja, Lambir, and Huai Kha Khaeng) lead to a slope of –0.31 (estimated by Gilbert et al. 2010).

Davis, M. A., Curran, C., Tietmeyer, A. & Miller A. Dynamic tree aggregation patterns in a species-poor temperate woodland disturbed by fire. *J Veg Sci.* **16**, 167-174 (2005). Log(Ω_{0-10}) values were plotted against Log(abundance), (Fig. 4), slope of -1.14, Cedar Creek's oak-woodland plot.

Du, H. et al. Spatial distribution of tree species in evergreen-deciduous broadleaf karst forests in southwest China. *Sci. Rep.* **7**: 15664. Plotted $g_{0\text{-}10}$ against Log(abundance) (Fig. 3), Mulun plot.

Flügge, A.J., Olhede, S.C. & Murrell, D.J. The memory of spatial patterns: changes in local abundance and aggregation in a tropical forest. *Ecology* **93**, 1540–1549 (2012). Plotted log (1+Ω_{0-10}) against log (abundance) (Fig. 2), BCI plot.

Gilbert, S. *et al.* Beyond the tropics: forest structure in a temperate forest mapped plot. *J Veg Sci.* 21, 388–405 (2010). Log(Ω_{0-10}) values were plotted against Log(abundance) and showed a slope of -0.82 (Fig. 4), University of California Santa Cruz -Forest Ecology Research Plot.

Gu, H., Li, J., Qi, G & Wang, S. Species spatial distributions in a warm-temperate deciduous broad-leaved forest in China. *J. For. Res.* **31**, 1187–1194 (2020). Plotted Ω_{0-10} values against Log(abundance) (Fig. 3), Donglingshan temperate plot.

Guo, Y., *et al.* Spatial distribution of tree species in a species-rich subtropical mountain forest in central China. *Can. J. For. Res.* **43**, 826–835 (2013). Plotted Ω_{0-10} against log(abundance) (Fig. 4), Badagongshan (BDGS) plot.

Li, L., *et al.* Spatial distributions of tree species in a subtropical forest of China. *Oikos* **118**, 495–502 (2009). Condit's Ω_{0-10} values were plotted against Log(abundance) (Fig. 3), Dinghu plot.

Morlon, H. *et al.* A general framework for the distance–decay of similarity in ecological communities. *Ecol. Lett.* **11,** 904–917 (2009). $Log_{10}(\Omega_{0-10})$ values were plotted against Log_{10}(abundance) (Fig. 5d), the slopes for the Yasuni, Korup, and BCI plots were -0.19, -0.31, and -0.32, respectively.

Perry, G.L.W., Enright, N.J., Miller, B.P. & Lamont, B.B. Do plant functional traits determine spatial pattern? A test on species-rich shrublands, Western Australia. *J. Veg. Sci.* **24**, 441–452 (2013). Did not find clear relationships between aggregation (measured using the pair correlation function) and abundance, four shrubland plots in Western Australia.

Song, H. *et al.* Investigating distribution pattern of species in a warm-temperate conifer-broadleaved-mixed forest in China for sustainably utilizing forest and soils. *Sci. Tot. Env.* **578**, 81–89 (2017). Ω_{0-10} decreased significantly as abundance increased (Fig. 3), plotted Ω_{0-10} against log(abundance), Lingkong plot.

Umaña, M.N. *et al.* The role of functional uniqueness and spatial aggregation in explaining rarity in trees. *Glob. Ecol. Biogeogr.* **26,** 777–786 (2017). Standardized effect size (SES) of Condit's Ω_{0-10} values were plotted against Log(abundance) (Fig. 3). Lilly Dickey Woods, Wabikon, Changbaishan, Fushan, Luquillo, Guanacaste, Gutianshan, and Xishuangbanna plots.

Wang X. et al. Spatial distributions of species in an old-growth temperate forest, northeastern China. *Can. J. For. Res.* **40**, 1011–1019 (2010). Ω_{0-10} values were plotted against Log(abundance) (Fig. 3), Changbaishan plot.

Wiegand, T. *et al.* Consequences of spatial patterns for coexistence in species-rich plant communities. *Nat. Ecol. Evol.* **5**, 965–973 (2021). Used $K(r)/\pi r^2$ for r = 10m, which is the same as Condit's Ω_{0-10} and plotted log(Ω_{0-10})against log(abundance) (Extended Data Fig. 8). Used 8 ForestGEO plots that are also included in the current analysis, and two simulated data sets.

Zhang, H., Gilbert, B., Wang, W., Lui, J. & Zhou, S. Grazer exclusion alters plant spatial organization at multiple scales, increasing diversity. *Ecology and Evolution* **3**, 3604-3612 (2013). Aggregation-abundance power laws in grass ramets (Fig. 3), with exponents between -0.4 and -0.455.

Zhang, Z., Hu, G., Zhu, J, & Ni, Z. Aggregated spatial distributions of species in a subtropical karst forest, southwestern China. *J. Plant Ecol.* **6**, 131–140 (2013). Ω_{0-10} values were plotted against Log(abundance) (Fig. 3), Maolan plot.

Details of the spatial analysis

Decomposition of average crowding indices

The task is to relate the neighbourhood-scale averages of the crowding indices $\overline{C_{kf}}$ and $\overline{H_{kf}}$ shown in Box 1 to the population-scale abundances N_f and measures of spatial patters (i.e., conspecific aggregation and heterospecific segregation). We solve this up-scaling problem using point-process theory (Wiegand and Moloney 2014; Illian et al. 2008). Before we explain how we obtain equations 6a and 6b in the main text, we present some basics of spatial point process theory and a simpler example of a crowding index (Wiegand et al. 2021) that leads to the aggregation measure Ω_{0-10} presented in Condit et al. (2000).

In the simplest case, an index of conspecific crowding simply counts the number of neighbours within distance r of the focal individual (Wiegand et al. 2021). This leads to Ripley's K-function, a well-known quantity in spatial statistics. The K-function can be estimated as the expected number of neighbours occurring within distance r of the typical individual, divided by λ_f, the overall density of a species in the plot (i.e., $\lambda_f = N_f/A$, the number N_f of individuals divided by the area A of the plot). Thus, in the simplest case, the conspecific crowding index is given by $\lambda_f K(r)$.

Spatial aggregation describes the extent to which trees of the same species tend to occur in spatial clusters and is usually defined as the average density of conspecific trees in circular neighbourhoods around each individual tree, divided by the mean density of the species across the whole plot (Condit et al. 2000; Wiegand and Moloney 2014).Using the K-function, we obtain with this definition the measure of aggregation $k_{ff}(r) = K(r)/\pi r^2$. If there is an excess of neighbours within distance r (i.e., $k_{ff}(r) > 1$) we have aggregation, and if there are fewer than expected neighbours, we have regularity (i.e., $k_{ff}(r) < 1$).

We can now decompose our simple crowding index $\lambda_f K(r)$ into the measure $k_{ff}(r)$ of aggregation and species abundance N_f, given that $\lambda_f = N_f/A$ we obtain

$$\lambda_f K(r) = N_f \frac{\pi r^2}{A} k_{ff}(r) \qquad \text{(S1)}$$

where the quantity $\pi r^2/A$ is a scaling constant that scales the number of individuals from the entire plot with area A to the neighbourhood with area πr^2.

To decompose our crowding indices that additionally weight each individual by 1 over distance to the focal individual, we first recognize that the K-function is the cumulative version of the pair correlation function $g(r)$:

$$K(r) = \int_0^r g(r)\, 2\pi r\, dr. \qquad \text{(S2)}$$

The quantity $\lambda_f g(r)$ is the density of points within a ring with radius r and width dr, centred at the typical individual, and multiplying with the area of that ring

(=$2\pi r\ dr$) yields the expected number of neighbours in this ring. Summing up over all rings up to radius r gives the expected number of neighbours occurring within distance r of the typical individual (i.e., $\lambda_f K(r)$). The pair correlation function is normalized in a way that it has a value of $g(r) = 1$ if the neighbourhood density is identical to the overall density λ_f of individuals in the plot (= N_f/A). Thus, the value of one of the pair correlation function serves as dividing line between cases of aggregation where $g(r) > 1$ (i.e., the typical individual has more neighbours than expected at distance r by a random distribution) and cases of regularity where $g(r) < 1$ (i.e., the typical individual has less neighbours than expected at distance r by a random distribution).

Taking advantage of equation S2, we write the distance-weighted conspecific crowding index as

$$\overline{C_{kf}} = \frac{N_f}{A}\int_0^r \frac{g(r)}{r} 2\pi r\ dr. \quad \text{(S3)}$$

We can do this since the pair correlation function looks only at neighbours at distance r of the typical individual. The r cancels, and with small rearrangements and adding factor r ($1/r$) we obtain the decomposition of the conspecific crowding index (equation 6a in the main text):

$$\overline{C_{kf}} = N_f \left(\frac{2\pi r}{A}\right)\left[\frac{1}{r}\int_0^r g(r)\ dr\right]. \quad \text{(S4)}$$

into abundance N_f, a scaling constant $c = 2\pi r/A$, and our measure of aggregation

$$k_{ff}(r) = \frac{1}{r}\int_0^r g(r)\ dr, \quad \text{(S5)}$$

which is the average of the pair correlation function up to distance r. The measure $k_{ff}(r)$ has the desired properties of a measure of aggregation, if the average neighbourhood density of conspecific trees equals the mean density of the species across the whole plot, we obtain $g(r) = 1$ and therefore $k_{ff}(r) = 1$, if the number of neighbours is larger we obtain $g(r) > 1$ (= aggregation) and if the number of neighbours is smaller we obtain $g(r) < 1$ (= regularity).

In the same way we obtain the scaling relationship for the heterospecific crowding index $\overline{H_{kf}}$ that counts the (distance-weighted) number of heterospecific neighbours within distance r of the typical individual of the focal species f. Here we use for the decomposition the bivariate pair correlation function $g_{fh}(r)$, the density of heterospecific neighbours at a small distance interval ($r–dr/2$, $r+dr/2$) of the typical individual of the focal species f, divided by the overall density λ_h of heterospecifics:

$$\overline{H_{kf}} = \sum_{i\neq f} \frac{(\sum_{i\neq f} N_f)}{A}\int_0^r \frac{g_{fh}(r)}{r}\ 2\pi r\ dr, \quad \text{(S6)}$$

which results in the decomposition (equation 6b):

$$\overline{H_{kf}} = \left(\sum_{i\neq f} N_f\right)\left(\frac{2\pi r}{A}\right)\left[\frac{1}{r}\int_0^r g_{fh}(r)\,dr\right]. \quad \text{(S7)}$$

into the sum of the abundances of heterospecifics $\sum_{i\neq f} N_f$, the scaling constant $c = 2\pi r/A$, and our measure of segregation

$$k_{fh}(r) = \frac{1}{r}\int_0^r g_{fh}(r)\,dr, \quad \text{(S8)}$$

the average of the bivariate pair correlation function up to distance r. The measure $k_{fh}(r)$ has the desired properties of a measure of segregation, defined as the degree of reduction of heterospecific neighbours, compared to the expectation of a independent species distribution: if the focal species is located independently on heterospecifics, we obtain $g_{fh}(r) = 1$ and therefore $k_{fh}(r) = 1$, if the number of heterospecific neighbours is smaller than expected we obtain $k_{fh}(r) < 1$ (= segregation) and if the number of heterospecific neighbours is larger we obtain $k_{fh}(r) > 1$ (= attraction).

To obtain the scaling relationship for the crowding index $\overline{I_{kf}}$ that weight additionally to $\overline{H_{kf}}$ each heterospecific neighbour by its relative interaction strength β_{fi}/β_{ff} we first define the quantity

$$B_f = \overline{I_{kf}}/\overline{H_{kf}}, \quad \text{(S9)}$$

the average competition strength of one heterospecific neighbour relative to that of one conspecific. We found that the quantity B_f is for species rich forests at or near a stationary state in good approximation a species-specific constant (see Supplementary Text in Wiegand et al. 2021). Thus, we can apply a mean-field approximation (O'Dwyer and Chisholm 2014; Fung et al. 2022) where the species-specific competition strengths of heterospecifics can be replaced by an average heterospecific competition strength, the quantity B_f. The B_f summarizes the emerging effects of the individual-level interaction coefficients β_{fi}/β_{ff} at the population-level. Note that this approximation does not mean that we ignore differences in pairwise interaction strength at the individual level, where competitive interactions occur, but the approximation tells us that the effect of existing differences in pairwise interactions strengths between species average out at the community level.

Using equation S9, we can decompose the crowding index $\overline{I_{kf}}$ together with equation S7 into

$$\overline{I_{kf}} = B_f\overline{H_{kf}} = k_{fh}\,B_f\,(c\sum_{i\neq f} N_i) \quad \text{(S10)}$$

Given that strong local density dependence causes approximate zero-sum dynamics, where the total number J of individuals remains constant, we can approximate the number of heterospecifics in equation S10 by $J - N_f$ and obtain the final decomposition (eq. 6c):

$$\overline{I_{kf}} = c\,k_{fh}\,B_f\,(J - N_f) \quad \text{(S11)}$$

Using these approximations decouples the multispecies dynamics and allows us to investigate the dynamics of individual species in good approximation.

When estimating the crowding indices and the indices of spatial patterns from the data, we need to conduct edge correction. This is because individuals too close to the edge of the plot do not have complete neighbourhoods with radius r inside the plot. We can therefore not evaluate their number of con- and heterospecific neighbours. To avoid bias, we excluded these individuals.

Model equations for alternative models

In equation 7 we present a simple macroscale model where neighbourhood crowding governs the survival of individual adult trees. However, the neighbourhood crowding can also affect reproduction (i.e., the number of offspring produced per adult) or establishment of offspring (i.e., whether or not an offspring placed at a given location can establish). In the following we present several alternative models with neighbourhood crowding in adult survival, offspring survival and reproduction.

Alternative Model A1: Density dependence in reproduction due to neighbourhood crowding

The spatially-enriched macroscale model for the per capita growth rate of species f with neighbourhood crowding affecting reproduction is given by

$$\tilde{\lambda}_f(N_{f,t}) = \frac{N_{f,t+1}-N_{f,t}}{\Delta t}\frac{1}{N_{f,t}} = r_f e^{-\beta_{ff} W_f(N_{f,t})} - d_f \qquad \text{(S12)}$$

where r_f is the maximal reproduction rate (at a location without crowding competition were the fitness factor $W_f = 0$), d_f is the average per capita mortality rate of adults obtained from the data, β_{ff} the individual-level conspecific interaction coefficients of species f, and $W_f(N_{f,t})$ the fitness factor of equations (7). Note that the crowding indices count, similar to the case were neighbourhood crowding affects survival, conspecific and heterospecific neighbours around adult individuals. Assuming approximate equilibrium, we obtain from equation S12 the unknown value of the individual-level conspecific interaction coefficients β_{ff} as: $\beta_{ff} = -\ln(\frac{d_f}{r_f})/W_f(N_f^*)$.

The corresponding full birth-death model is therefore given by

$$\text{birth rate:} \quad b_n = (n\, e^{-\beta_{ff} W_f(n)} + v) r_f\, d\tau \qquad \text{(S13a)}$$

$$\text{death rate:} \quad d_n = n\, d_f\, d\tau \qquad \text{(S13b)}$$

and the approximation of the birth rate at a typical small abundance N_s is given by

$$\tilde{b}_n = n(b_f + v)d\tau \qquad \text{(S13c)}$$

where $b_f = r_f e^{-\beta_{ff} W_f(N_s)}$. Note that $\tilde{\lambda}_f(N_s) = b_f - d_f$. The extinction risk for the linear birth-death process (equations 13b,c) is given by

$$P_0(t, N_0) = \left[\frac{b_f - d_f}{b_f \Delta - d_f}\right]^v \left(\frac{d_f \Delta - d_f}{b_f \Delta - d_f}\right)^{N_0}, \qquad \text{(S14a)}$$

where $\Delta = e^{(b_f - d_f)t}$. We now define $x = \tilde{\lambda}_f(N_s)/d_f = b_f/d_f - 1$ and $T = d_f t$ being the time scaled by the mean mortality rate, and obtain $\Delta = e^{xT}$ and

$$P_0(x, T, N_0) = \left[\frac{x}{(x+1)e^{xT} - 1}\right]^v \left(\frac{e^{xT} - 1}{(x+1)\, e^{xT} - 1}\right)^{N_0}, \qquad \text{(S14b)}$$

Equation S14b can be directly compared to equation 2 in the main text.

Alternative model A2: Density dependence in establishment of offspring

The equations for alternative model A1 above apply also for the case where neighbourhood crowding affects the establishment of offspring after it is placed at a given location. This is because in model A1 the number of established recruits is reduced by distributing less recruits that then always establish (i.e., on average $r_f N_{f,t}\, e^{-\beta_{ff} W_f(N_{f,t})}$ recruits are distributed), whereas in model A2 $r_f N_{f,t}$ recruits are distributed on average, and then, depending on their neighbourhood, they can establish with probability $e^{-\beta_{ff} W_f(N_{f,t})}$). However, in model A2, the crowding indices need to count conspecific and heterospecific neighbours around the locations of the tentative offspring. For example, the conspecific crowding index C_{kf} is then given by the (distance-weighted) number of conspecific adults located within distance r of an offspring individual k. This somewhat complicates the estimation of the crowding indices and indices of spatial patterns, because only the fraction $r_f N_f$ of focal individuals (i.e., tentatively placed recruits) can be used to estimate the average crowding and pattern indices, whereas in the alternative model A1 (and the model of equation 7) we have 10 time more focal individuals (i.e., adults) to estimate the indices, if r_f (or d_f) = 0.1.

In the alternative model A2 we expect a trade-off behaviour of stabilisation in response to changing the rules of placement of offspring relative to their parents. In the one extreme, when offspring is placed close to their parents, a negative relationship between aggregation and abundance will arise as in our model (eq. 7) and reduce stabilisation. However, in the other extreme, when offspring is placed in an aggregated way away from their parents, the corresponding aggregation index

(which is now not adult aggregation, but aggregation of adults around tentative offspring) will approach values of one because offspring is placed independently on the locations of their parents. This leads to low stabilisation. We expect that maximal stabilisation will be reached if a certain proportion of offspring remains close to the parents (e.g., $b_f = -0.4$) and/or the random cluster centres around which offspring is placed persist more than one census period.

Alternative model A3: Density dependence in reproduction and mortality due to neighbourhood crowding

This spatially-enriched macroscale model corresponds to the classical Lotka-Volterra model and is given by

$$\tilde{\lambda}_f(N_{f,t}) = r_f\,(1 - \beta_{ff} W_f(N_{f,t})) - m_f\,\beta_{ff} W_f(N_{f,t}) \qquad \text{(S15)}$$

where r_f and m_f are the per capita reproduction and mortality rates without crowding competition (i.e., $W_f(N_{f,t}) = 0$), respectively, and $W_f(N_{f,t})$ is the fitness factor of equations (7). Assuming approximate equilibrium, we obtain from equation S15 the unknown value of the individual-level conspecific interaction coefficients $\beta_{ff} = \frac{r_f}{r_f + m_f} \frac{1}{W_f(N_f^*)}$.

The corresponding full birth-death model is therefore given by

$$\text{birth rate:} \qquad b_n = (n\{1 - \beta_{ff} W_f(n)\} + v) r_f\, d\tau \qquad \text{(S16a)}$$

$$\text{death rate:} \qquad d_n = n\{\beta_{ff} W_f(n)\}\, m_f\, d\tau \qquad \text{(S16b)}$$

and we approximation of the birth and death rate at a typical small abundance N_s is given by

$$\tilde{b}_n = n(b_f + v) d\tau \qquad \text{(S17c)}$$

$$\tilde{d}_n = n\, d_f\, d\tau \qquad \text{(S17c)}$$

where $b_f = r_f\{1 - \beta_{ff} W_f(N_s)\}$ and $d_f = m_f\{\beta_{ff} W_f(N_s)\}$. Note that $\tilde{\lambda}_f(N_s) = b_f - d_f$. The extinction risk for the linear birth-death process (equations 13b,c) is given by

$$P_0(t, N_0) = \left[\frac{b_f - d_f}{b_f \Delta - d_f}\right]^v \left(\frac{d_f \Delta - d_f}{b_f \Delta - d_f}\right)^{N_0}, \qquad \text{(S18a)}$$

where $\Delta = e^{(b_f - d_f)t}$. With the definitions $x = \tilde{\lambda}_f(N_s)/d_f = b_f/d_f - 1$ and $T = d_f t$ we obtain $\Delta = e^{xT}$ and therefore as in equation S14b:

$$P_0(x, T, N_0) = \left[\frac{x}{(x+1)\, e^{xT} - 1}\right]^v \left(\frac{e^{xT} - 1}{(x+1)\, e^{xT} - 1}\right)^{N_0}. \qquad \text{(S18b)}$$

Note that in this case the scaled time T depends via the death rate d_f on the typical small abundance N_s.

Spatially-explicit simulation model

Model description (adapted from Wiegand et al. 2021)

The individual-based simulations serve two main purposes; first, they are used to verify that the observed patterns (i.e., the abundance-aggregation power law) can emerge in principle from the minimal mechanisms included into the macroscale model, and they are used as "known data" to test if the parameterized birth-death model (equations 12 and 13) is able to predict the simulated abundance distribution correctly.

The model is an individual-based and stochastic implementation of the spatial multi-species model (equations 1, 7a), and simulates the dynamics of a community of initially S tree species (in our case S = 80) in a given plot of a homogeneous environment (in our case 200 ha) in 5-year timesteps adapted to the ForestGEO census interval. Only reproductive (adult) trees are considered, but no size differences.

During a given 5 yr timestep the model simulates first stochastic recruitment of reproductive trees and placement of recruits, and second, stochastic survival of adults (equation 4) depending on the neighbourhood crowding indices for conspecifics (C_{kf}) and heterospecifics (H_{kf} or I_{kf} depending on the scenario) (but excluding recruits)(equation 3). In the next timestep the recruits count as reproductive adults and are subject to mortality. No immigration from a metacommunity is considered. To avoid edge effects torus geometry is assumed.

The survival probability of an adult k of species f is given by equation (4) and yields $s_{kf} = s_f \, exp(- \beta_{ff} (C_{kf} + I_{kf}))$. The two neighbourhood indices C_{kf} and I_{kf} describe the competitive neighbourhood of the focal individual k and sum up all conspecific and heterospecific neighbours within distance r, respectively, but weight them by the inverse of it distance to the focal individual k and by the relative individual-level interaction coefficients β_{fi}/β_{ff}. If con- and heterospecifics compete equally at the individual-scale, we have $\beta_{fi} = \beta_{ff}$.

Each individual produces r_f recruits on average and their locations are determined by a type of Thomas process (Wiegand and Moloney 2014) to obtain a clustered distribution of recruits. In our model, the spatial position of the recruits is determined by two independent mechanisms. First, a proportion $1–p_d$ of recruits is placed stochastically around randomly selected conspecific adults (parents) by using a two-dimensional kernel function (here a Gaussian with variance σ^2). This is the most common way in most spatially-explicit models to generate species clustering. Technically, we first select for each of these recruits randomly one parent among the conspecific adults and then determine the position of the recruit by sampling from the kernel. Second, the remaining proportion p_d of recruits is distributed

in the same way around randomly placed cluster centres that are located independently of conspecific adults. We select first for each of these recruits randomly one cluster centre among the cluster centres of the corresponding species, and then determine the position of the recruit by sampling from the kernel.

Parameterization of the simulation model

The simulation model used here is described in Wiegand et al. (2021). In contrast to Wiegand et al. (2021), we use here distance-weighting for the estimation of the crowding indices. Thus, in the source code (published as Supplementary information in Wiegand et al. 2021) we use now DistanceWeighting = 1 instead of DistanceWeighting = 0.

The simulations of the simple individual-based forest model were conducted over 25,000 yrs (= 5000 census periods) in an area of A = 200 ha, and comprised approximately 86,000 trees with initially 80 species. There was no immigration. The model parameters were the same for all species, and all species followed exactly the same model rules. We selected $\beta_{fi} = \beta_{ff}$ to obtain no differences in con- and heterospecific interactions and $s_f = 1$ (no background mortality), and we adjusted the parameters $\beta_{ff} = 0.02$ and $r_f = 0.1$ to yield tree densities (430/ha) and an overall 5 year mortality rate (10%) similar to that of trees with dbh ≥ 10cm of the BCI plot[71]. The radius of the neighbourhood used to estimate the crowding indices was r = 15m.

To test if the birth-death model is able to correctly predict the species abundance distribution of the individual-based implementation of our model, we selected three different parameterizations of the placement of recruits that produce typical average individual fitness functions (Fig. S1a). To this end we used for the three parameterizations respective values of σ = 67, 15, 10m for the parameter σ of the Gaussian kernel that places recruits around conspecific adults or around randomly placed cluster centres. We obtain weak spatial aggregation for σ = 67 and stronger smaller-scale aggregation for the values σ =15, 10 m to mimic more realistic seed dispersal distances (Wiegand et al. 2017). The probabilities p_d that a new recruits was located close to one of the randomly placed cluster centres were p_d = 0.0125, 0.6, and 1, respectively, while the probability to be placed close to a conspecific adult was 1 - p_d. We used in our simulations 16 random cluster centres that changed every timestep their location.

Characteristics of the model scenarios

The first scenario represents a case of weak aggregation (σ = 67m). It results in the

power law $PL(N_f) = 6.2\ N_f^{-0.999}$ with an average individual fitness functions of almost zero for all abundances (Fig. S1a, top), and the birth-death mode predicts after 5000 census periods Δt a very wide probability distribution $P_n(t)$ (Fig. S1b, top). The second scenario represents realistic aggregation (σ = 15m) with recruits placed in similar proportions around their parents and randomly selected cluster centres. It results in the power law $PL(N_f) = 2.9\ N_f^{-0.327}$ with a moderate average individual fitness functions at lower abundances (Fig. S1a, middle), and a much narrower distribution $P_n(t)$ (Fig. S1a, middle). The third scenario represents strong aggregation (σ = 10m) with recruits placed only around the randomly selected cluster centres. It results in the power law $PL(N_f) = 1.6\ N_f^{-0.0013}$ with a high average individual fitness functions at low abundances (Fig. S1a, bottom) and a narrow distribution $P_n(t)$ (Fig. S1b, bottom). In all cases, the probability distribution $P_n(t)$ predicted by the birth-death model matched the abundance distribution of the individual-based simulations after 5000 census periods well (Figure 1c).

References

Condit, R. *et al.* Spatial patterns in the distribution of tropical tree species. *Science* **288**, 1414–1418 (2000).

Fung, T. O'Dwyer, J. & Chisholm, R. Effects of temporal environmental stochasticity on species richness: a mechanistic unification spanning weak to strong temporal correlations. *Oikos* e08667 (2022).

Illian, J., Penttinen, A., Stoyan, H. & Stoyan, D. *Statistical Analysis and Modelling of Spatial Point Patterns* (Wiley, 2008).

O'Dwyer, J. & Chisholm, R. A mean field model for competition: From neutral ecology to the Red Queen. *Ecol. Let.* 17: 961–969 (2014).

Wiegand, T. *et al.* Consequences of spatial patterns for coexistence in species-rich plant communities. *Nat. Ecol. Evol.* **5**, 965–973 (2021).

Wiegand, T., May, F., Kazmierczak, M. & Huth, A. 2017. What drives the spatial distribution and dynamics of local species richness in tropical forest. *Proc. R. Soc. B* **284**, 20171503.

Wiegand, T. & Moloney, K. A. *A handbook of spatial point pattern analysis in ecology*. (Chapman and Hall/CRC press, 2014).

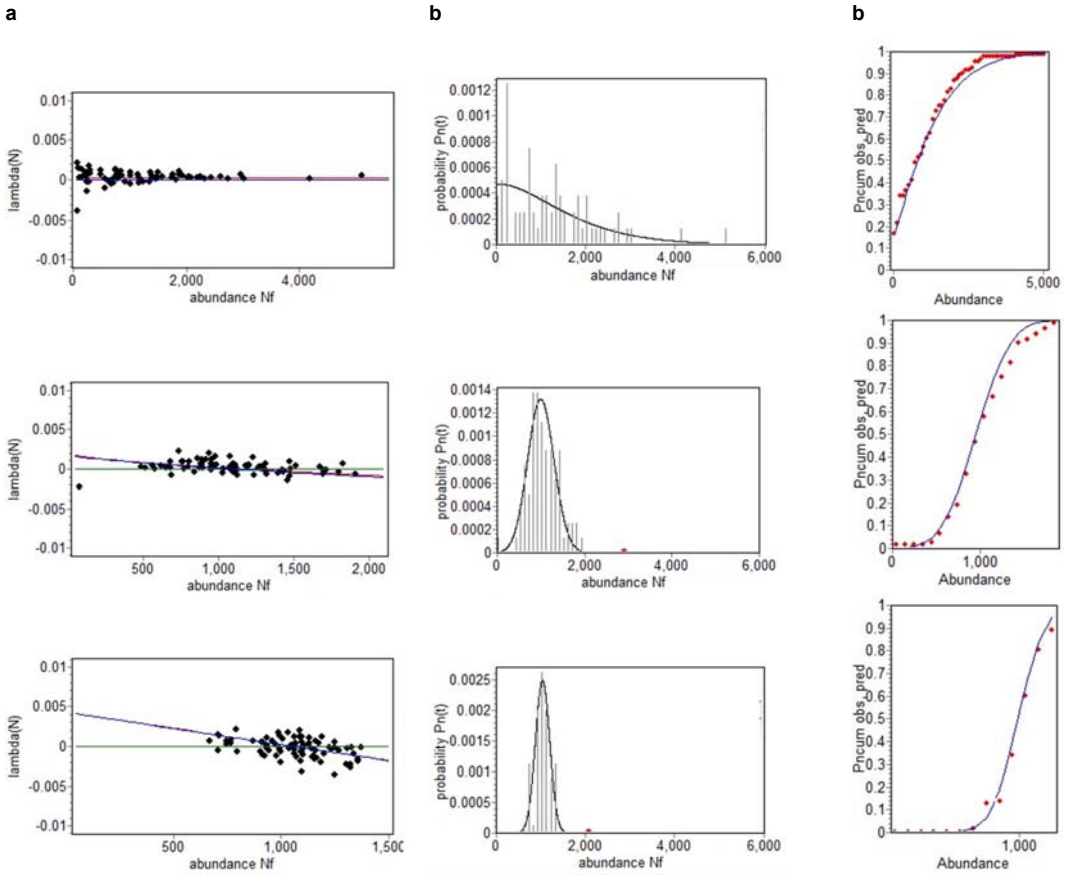

Figure S1. The birth-death model predicts the species abundance distribution of individual-based simulations. **a,** The average individual fitness (red-blue line) determined from the fitted power-law relationship between ($k_{ff} - k_{fh}$) and N_f(Extended Data Fig. 1), the mean value of k_{fh}, the observed total community size J, and the model parameters β_{ff} = 0.02, r_f = 0.1, and s_f = 1.0 (see methods). The black dots show the values of average individual fitness for the different species, given their observed abundance N_f^*, aggregation k_{ff} and segregation k_{fh}, **b**, The observed species abundance distribution of the individual-based model (IMB) after 25,000 years (bars) and the corresponding prediction of the birth-death model (black line), the (scaled) probability $P_n(t)$ that the species has at time t n individuals, **c**, The cumulative probability distributions (red dots: simulated by IBM, blue line: predicted by birth-death model). The individual-based simulation model is a spatially explicit and stochastic implementation of the spatial multi-species model (equation 1), and simulates the dynamics of a community of initially 80 tree species in a given 200 ha plot of a homogeneous environment in 5-year time steps.